4 **New particle formation in the Svalbard region 2006 - 2015**

6 Jost Heintzenberg[1], Peter Tunved[2], Martí Galí[3], and Caroline Leck[4]

9 1: Leibniz Institute for Tropospheric Research (TROPOS), Permoserstr. 15, 04318 Leipzig,

10 Germany

11 2: Department of Environmental Science and Analytical Chemistry (ACES), Stockholm

12 University, 10691 Stockholm, Sweden

13 3: Takuvik Joint International Laboratory & Québec-Océan, Université Laval, G1V 0A6

14 Québec, Canada

15 4: Department of Meteorology, Stockholm University (MISU), 10691 Stockholm, Sweden

17   Abstract

19   Events of new particle formation, (NPF), were analyzed in a ten-year data set of hourly

20   particle size distributions recorded on Mt. Zeppelin, Spitsbergen, Svalbard. Three different

21   types of NPF-events were identified through objective search algorithms. The first and

22   simplest algorithm utilizes short-term increases in particle concentrations below 25 nm,

23   (PCT-events). The second one builds on the growth of the sub-50 nm diameter-median,

24   (DGR-events), and is most closely related to the classical "banana-type" of events. The third

25   and most complex, so-called multiple-size approach to identifying NPF-events builds on a

26   hypothesis suggesting the concurrent production of polymer gel particles at several sizes

27   below about 60 nm, (MEV-events).

28   As a first and general conclusion we can state that NPF-events are a summer phenomenon

29   and not related to Arctic haze, which is a late winter-to-early spring feature. The occurrence

30   of NPF-events appears to be somewhat sensitive to the available data on precipitation. The

31   seasonal distribution of solar flux suggests some photochemical control that may affect

32   marine biological processes generating particle precursors and/or atmospheric photochemical

33   processes that generate condensable vapors from precursor gases. Notable, the seasonal

34   distribution of the biogenic methanesulfonate, (MSA), follows that of the solar flux although

35   it peaks before the maxima in NPF-occurrence.

36   A host of ancillary data and findings point to varying and rather complex marine biological

37   source processes. The potential source regions for all types of new particle formation appear

38   to be restricted to the marginal ice and open water areas between Northeastern Greenland and

39   Eastern Svalbard. Depending on conditions yet to be clarified new particle formation may

40   become visible as short bursts of particles around 20 nm, (PCT-events), longer events

41   involving condensation growth, (DGR-events), or extended events with elevated

42   concentrations of particles at several sizes below 100 nm, (MEV-events). The seasonal

43   distribution of NPF-events peaks later than that of MSA and, DGR and in particular of MEV-

44   events reach into late summer and early fall with much open, warm, and biologically active

45   waters around Svalbard. Consequently, a simple model to describe the seasonal distribution

46   of the total number of NPF-events can be based on solar flux, and sea surface temperature,

47   representing environmental conditions for marine biological activity, and condensation sink,

48   controlling the balance between new particle nucleation and their condensational growth.

49   Based on the sparse knowledge about the seasonal cycle of gel-forming marine

50   microorganisms and their controlling factors we hypothesize that the seasonal distribution of

51   DGR and more so MEV-events reflect the seasonal cycle of the gel-forming phytoplankton.

1. Introduction

In the late 1970s and early 1980s the interest in the Arctic atmospheric aerosol widened from the well-identified winter phenomenon of Arctic haze (Rahn and Shaw, 1977; Heintzenberg and Leck, 1994) to summer conditions in this northernmost remote region. In the pristine Arctic summer air the so-called background aerosol (Junge, 1963) was expected to be most clearly visible, far away from the northern hemispheric anthropogenic emission centers at lower latitudes. Episodic and localized occurrences of high concentrations of ultrafine particles, (here defined as particles with diameters < 100 nm), in the summer Arctic were explained by rare import of polluted air from lower latitudes (Flyger and Heidam, 1978; Heintzenberg and Larssen, 1983) or hypothetical anthropogenic sources in the Arctic (Jaenicke and Schütz, 1982).

With the advent of sensitive condensation nuclei counters (Agarwal and Sem, 1980) and differential mobility analyzers (Knutson and Whitby, 1975a, b) more details became visible in the Arctic sub-micrometer aerosol. High numbers of ultrafine particles were observed in connection with fog passages (Lannefors et al., 1983) and chemical aerosol information indicated a regional – possibly biogenic – particle sources in the summer Arctic (Heintzenberg, 1989). The high molar ratios of methane sulfonate, (MSA), to non-sea salt sulfate, (nssSO$_4^{2-}$), of 0.28 in the Arctic summer aerosol found by Heintzenberg and Leck (1994) substantiated the biogenic source of the particles.

The establishment of long-term Arctic aerosol monitoring at the fringes of the pack ice in Alaska (e.g., Polissar et al., 1999), Canada (e.g., Norman et al., 1999; Willis et al., 2016), and on Spitsbergen (e.g., Tunved et al., 2013) revealed more details of potential sources of the summer aerosol, in particular their connection to the marine biosphere in the Arctic. The unique series of systematic aerosol studies in the central Arctic north of 80°N onboard the Swedish icebreaker *Oden* in 1996 led to the formulation of a new hypothesis concerning a

80   specific process of marine biogenic particle formation (Leck and Bigg, 1999). The marine

81   biogenic particles involved behaved as polymer gels and originated in the surface microlayer

82   (SML) of the ocean, (Orellana et al., 2011b), from the activity of sea-ice algae,

83   phytoplankton and, perhaps, bacteria. The new particle events were reported to occur as

84   simultaneous enhancement of particle number concentrations in the whole size-range below

85   50 nm, and not with the prototypical "banana growth" (Kulmala et al., 2004). Two more

86   *Oden* cruises in 2001 and 2008 yielded results that were partly contradicting (Held et al.,

87   2011b; Held et al., 2011a), partly supporting the SML hypothesis (Leck et al., 2013; Karl et

88   al., 2013; Orellana et al., 2011b; Leck and Bigg, 2010). The synopsis of the results of four

89   *Oden* cruises of Heintzenberg et al. (2015) identified geographic regions of new particle

90   formation (NPF) in the inner Arctic while stressing the importance of recent open water and

91   related biological activity in the sea in transects by air masses with new particle formation

92   over the central Arctic.

93   Two years of aerosol size distributions from Mt. Zeppelin, Spitsbergen and Alert, both

94   located at the fringes of the central pack ice, were analyzed by Croft et al. (2016a) with a

95   global aerosol geophysics model. They discuss classical new-particle nucleation, coagulation

96   scavenging in clouds, scavenging by precipitation, and transport in order to explain the annual

97   cycle of the Arctic aerosol. Croft et al. (2016a) find two seasonal maxima in their modeled

98   particle nucleation rates, one in March, and one in July. In spring, their simulated NPF occurs

99   mainly in the free troposphere, whereas in summer, it occurs also in the planetary boundary

100   layer. More recently, Croft et al. (2016b) state that ammonia from seabird-colony guano is a

101   key factor contributing to bursts of newly formed particles, which are observed every summer

102   in the near-surface atmosphere, at least at Alert, Nunavut, Canada. Earlier, the results of

103   studies with another global aerosol model by Browse et al. (2014) suggested that the potential

104   increase in NPF in the Arctic with potential increases in cloud condensation nuclei is

105 compensated by wet scavenging. They also state that scavenging by pre-existing large

106 particles suppresses NPF-events.

107 Based on three years of data from the two Arctic sites Thule and Ny-Ålesund (gruvebadet)

108 Becagli et al. (2016) examined the sources and environmental factors controlling the

109 biological aerosol component MSA. Their analysis included satellite-derived Chlorophyll-*a*

110 (an indicator of phytoplankton biomass), oceanic phytoplankton primary productivity, (PPP),

111 and sea ice. Whereas they found good correlations between MSA, PPP and sea ice, (the latter

112 two being closely related), their data did not allow any statements on NPF processes.

113 To date the longest record of sub-micrometer number-size distributions of the Arctic

114 aerosol down to 5 nm particle diameter and below has been accumulated on Mt. Zeppelin,

115 Spitsbergen (Tunved et al., 2013; Heintzenberg and Leck, 1994). For the ten years from 2006

116 through 2015 a total of 63936 quality-controlled hours of aerosol data are available, i.e.

117 during 73% of all hours of the ten years. In the present study we exploit this formidable data

118 set in a search for processes forming new particles. An important first step in this work was

119 formulating completely objective criteria for the identification of events. In the relatively

120 clean Arctic environment we do not expect the classical nucleation and growth events as

121 frequently observed over the continents, (cf. Kulmala et al., 2004), to dominate. Thus, we

122 refrained from applying the objective search algorithm formulated by Heintzenberg et al.,

123 (2007) for this "Banana-type" of events. Instead we formulated new objective search

124 algorithms allowing several potential types of new particle formation events or formation

125 processes. With a host of complementary atmospheric and surface physical, chemical, and

126 biological information a large number of NPF-events identified with these algorithms will be

127 analyzed in the following chapters.

128

129

130

131 **2. Database**

132

133 The Mt. Zeppelin observatory

134

135 Situated at the top of Mt Zeppelin, Svalbard (78° 56'N, 11° 53'E), the Zeppelin observatory

136 offers a unique possibility to study the characteristic features of Arctic atmospheric

137 constituents such as trace gases and aerosol particles. At a height of 474 m a.s.l. the station is

138 located near the top of the local planetary boundary layer and represents remote Arctic

139 conditions. The closest source of pollution, the small community of Ny-Ålesund, is located

140 ~2 km north of the station

141 (http://www.esrl.noaa.gov/psd/iasoa/sites/default/files/stations/nyalesund/nyalesund_site.jpg).

142 However, the elevation difference and typical wind patterns largely prevent pollution from

143 nearby sources to reach the Zeppelin Observatory. The dominating wind pattern is east-

144 southeast katabatic flow from Kongsvegen glacier or from northwesterly directions as

145 channeled by the Kongsfjord (Beine et al., 2001; Heintzenberg et al., 1983). The station itself

146 was initially established in 1991, and is owned by the Norwegian Polar Research Institute

147 (NP). The Norwegian Institute for Air Research (NILU) is responsible for the coordination of

148 the scientific program.

149

150

151 **2.1 Physical aerosol data**

152

153 After a period of continuous aerosol measurements by the Department of Meteorology,

154 Stockholm University in the early 1990s, (Heintzenberg and Leck, 1994), the Department of

155 Analytical Chemistry and Environmental Science, Stockholm University, initialized

156 observations of the aerosol number size distribution in mid-2000. Originally, the system

157   consisted of a single differential mobility analyzer system, (DMPS), consisting of a medium-

158   size Hauke-type differential mobility analyzer, (DMA), together with a TSI 3760

159   condensation particle counter, covering diameters between 20 and ~500nm. From 2006 on

160   the particle size range was widened covering particle sizes between 10 and 790 nm. In 2005,

161   the rain-cover over the inlet was replaced. Initially, the instrument inlet was of a PM10 type,

162   removing particles or hydrometeors with diameters >10 μm from the sampled air stream.

163   During a substantial renewal of the Stockholm University equipment in 2010-2011, both inlet

164   and DMPS system were replaced.

165   Since then, the DMPS-system utilizes a custom-built twin DMA-setup comprising one

166   Vienna-type medium DMA (Reischl, 1991) coupled to a TSI CPC 3010 covering sizes

167   between 25-800 nm and a Vienna-type long DMA coupled with at TSI CPC 3772 covering

168   sizes between 5-60 nm. The size distributions from the two systems are harmonized on a

169   common size grid and then merged. Both systems use a closed-loop flow setup. The current

170   inlet hat is of whole air type, complying with EUSAAR[1] standard for high altitude or Arctic

171   sampling conditions. In the current setup, the inlet is operated with a flow of ca. 100 liters per

172   minute, (lpm). Laminar flow conditions apply throughout the sampling lines. Outside of the

173   station, the inlet temperature is kept above 0°C using active heating. Inside the station the

174   temperature increases gradually to room temperature (maximum temperature reaches ca. 25

175   °C, but remains typically around 20°C). Relative humidity, (RH) and temperature are

176   internally monitored and measurements are maintained at dry conditions with RH < 30%.

177   The system is regularly checked with latex spheres and flow controls. The recorded data are

178   manually screened and crosschecked with other available observation as in Tunved et al.

179   (2013). If inconsistencies were found between the different datasets, further investigation

---

[1] EUSAAR (European Supersites for Atmospheric Aerosol Research) is an EU-funded I3
(Integrated Infrastructures Initiatives) project carried out in the FP6 framework of the specific
research and technological development gram "Structuring the European Research Area -
Support for Research Infrastructures", (http://www.eusaar.net/files/data/data_protocol.cfm).

180 was performed to exclude data that were identified as affected by instrumental errors. Using
181 the instrumental logbook, periods of local activity potentially influencing the sampling were
182 also excluded from the dataset. During the years 2006 – 2010 no particles below 10 nm in
183 diameter were recorded. From 2011 on four more diameter bins down to 5 nm were included
184 and a different diameter array was utilized. To allow for a synopsis of all years all size
185 distributions were interpolated on the pre-2011 diameter array and all integrals of the size
186 distribution over particle diameter were taken over the joint diameter range 10 to 631 nm. For
187 the pre-2011 years the data at the four size channels below 10 nm were flagged as missing.
188 However, whenever results cover the complete time series the resulting number
189 concentrations in the four first channels covering the years 2011 – 2015 are carried along.

190 For the identification of NPF in terms of particle growth the parameter D50 in nanometer
191 was calculated as the number median diameter of particles smaller than 50 nm but larger than
192 10 nm, i.e. 50% of all particles below that size are smaller than D50. Besides this parameter
193 Table 1 lists nine integral particle parameters, which are utilized in the NPF-search
194 approaches or in the interpretation of results. These aerosol parameters quantify total particle
195 number, (NTO), and particle numbers in sub-ranges of the number size distribution such as
196 N25, quantifying the total number of particles between ten and 25 nm.

197 Following the concept developed by Pirjola et al., (1999), and Kulmala et al., (2001) we
198 calculated the condensation sink, (CS, s^{-1}), as a parameter with which the probability of new
199 particle formation from the gas phase and the necessary amount of condensable vapor can be
200 estimated. We utilized number size distributions, pressure and temperature taken from our
201 database for this calculation.

202

203

204

205

206   **2.2   Chemical aerosol data**

207

208   For the interpretation of NPF-events we employed chemical information derived from the

209   analyses of high volume particle samples taken by the Norwegian Institute for Air research,

210   (NILU). A high volume sampler (PM10) was used to collect samples for a quantitative

211   determination of sodium, (Na^+), sulfate, (SO_4^{2-}) and MSA (CH_3SOO^-). The sampler collected

212   material for analysis in one to three days. Blank samples were obtained by mounting the

213   glass fiber filters at the sampling site with the same sampling period but without air passing

214   through. Na^+ and SO_4^2 were analyzed by NILU and have been downloaded for the present

215   study from the EBAS database (http://ebas.nilu.no), which list details about the sampling

216   technique and the sampling protocol. Nss SO_4^{2-} was determined from total sulfate correcting

217   for sea salt sulfate as $0.25 \times Na^+$, (Keene et al., 1986).

218   MSA was analyzed at the laboratory of the Department of Meteorology, Stockholm

219   University. To allow for subsequent chemical determinations the ambient samples and blanks

220   were carefully handled in a glove box (free from particles, sulfur dioxide and ammonia). At

221   the time of the chemical analyses, still in the glove box, the substrates were extracted (in

222   centrifuge tubes) with 60 cm^3 deionized water (Millipore Alpha-Q, conductivity 18 MΩcm).

223   The extracts were thereafter analyzed for weak anions by chemically suppressed ion

224   chromatography (IC, Dionex ICS-2000) using Dionex AG11/AS11 columns. In order to trap

225   carbonates and other ionic contaminants a Dionex ATC-1 column was used before the

226   injection valve. The injection volume was 50 μdm^3. Quality checks of the IC-analyses were

227   performed with both internal and external reference samples (Das et al., 2011). The analytical

228   detection limits obtained for the various ions, defined as twice the level of peak-to-peak

229   instrument noise, was 0.0001 $\mu eq\ dm^{-3}$ for MSA. The overall analytical accuracy was better

230   than 1.5%.

231

232 **2.3 Back-trajectories and meteorological data**

233

234 For every hour during the ten years 2006 through 2015 three-dimensional back trajectories

235 have been calculated arriving at 474 m at Mt. Zeppelin. The trajectories have been calculated

236 backward for up to ten days using the HYSPLIT4 model (Draxler and Rolph, 2003) with

237 meteorological data from the Global Data Assimilation System with one-degree resolution

238 (GDAS1). Trajectories extending backwards for ten days are inaccurate at origin due to the

239 trajectory uncertainty of 25-30% of its length, (Stohl, 1998). More information about the

240 GDAS dataset can be found at Air Resources Laboratory (ARL), NOAA

241 (http://ready.arl.noaa.gov), from which the meteorological data were downloaded.

242 During the analyzed time period meteorological records at the Mt. Zeppelin station are

243 rather limited in quality and were frequently interrupted. There are no precipitation

244 measurements and wind measurements are strongly influenced by the station building and by

245 the local topography. In order to have an internally consistent, and unbroken meteorological

246 record we utilized hourly meteorological parameters at trajectory arrival times as calculated

247 by the HYSPLIT4 model. We emphasize that their accuracy depends on the quality of the

248 meteorological model inside HYSPLIT4 and the accuracy and representativeness of the

249 meteorological fields utilized by the model. Of the local meteorological record air

250 temperature was considered the most reliable and thus explored in a comparison of trajectory

251 calculated and modeled meteorological data. When comparing the 42600 contiguous hourly

252 records from 2008-01-01 until 2012-11-10 the average ratio of measured and calculated

253 temperatures is 0.98, with a coefficient of determination of 0.96. The utilized model

254 parameters are listed in Table 1.

255 As an additional parameter we evaluated the vertical air movement of the trajectories

256 during the last hour before arrival by subtracting the trajectory height one hour before arrival

257   at the arrival height of 474 meter. The resulting vertical displacement parameter, DZ, is given

258   in meters per hour. Positive values of DZ indicate a lifting of the air.

259   The most important missing meteorological information concerns the local cloud cover.

260   No direct recording was available of times during which the station was in clouds. The

261   closest available cloud instrument is a ceilometer operated by the Alfred Wegener Institute

262   (AWI) at their Koldewey Station in Ny-Ålesund, i.e. in the valley below Mt. Zeppelin, some

263   2.8 km of horizontal distance from the position of the mountain station. From the one-minute

264   records of the ceilometer we derived hourly values of the 25% percentile of cloud base, which

265   was used as an indicator for the Zeppelin station being in cloud. This ceilometer parameter is

266   listed as C25 in Table 1.

267   Precipitating clouds scavenge the planetary boundary layer and thus reduce the available

268   particle surface as condensation sink of particle precursors. As a consequence nucleation

269   from the gas phase may be facilitated (Tunved et al., 2013). As in Tunved et al. (2013) we

270   utilized the HYSPLIT-modeled precipitation along the back trajectories. Sums of

271   precipitation, (SP, see Table 1), were calculated along each back trajectory and will be

272   referred to as SP1 (during the last day), SP2 (during the last but one day), and SP5 (during

273   days three to five) before arrival at Mt. Zeppelin.

274

275

276   **2.4   Marine biological data**

277

278   The biologically active marginal ice zone is a major natural source of sulfur in the Arctic

279   summer atmosphere, (Leck and Persson, 1996b, a), and Wiedensohler et al. (1996), indicated

280   a potentially important role of dimethyl sulfide (DMS) in regional new particle formation.

281   DMS emissions from the sea have long been proposed to control new particle formation in the

282   marine boundary layer, (Charlson et al., 1987), which builds on DMS_{aq} being transported via

283   turbulence and diffusion to the sea-air interface, represented by the transfer velocity, which in

284   turn depends on sea-surface temperature, salinity, and wind speed, (Liss and Merlivat, 1986).

285   Once in the atmosphere DMS_g is photochemical oxidized via intermediates such as sulfuric

286   acid and methane sulfonic acid, (Ayers et al., 1996), which eventually leads to the formation

287   of aerosol $nssSO_4^{2-}$ and MSA. The products of the photochemical oxidation of DMS the ratio

288   MSA/ $nssSO_4^{2-}$ show a temperature dependence (Bates et al., 1990), favoring MSA in the cold

289   Arctic environment (Karl et al., 2007).

290   Dimethyl sulfide in the ocean (DMS_{aq}) is produced through the degradation of its algal

291   precursor dimethylsulfoniopropionate (DMSP) by microbial food webs, (Simó, 2001). At

292   high latitudes, total DMSP (DMSPt) and therefore DMS_{aq}, essentially follows the seasonal

293   cycle of phytoplankton biomass, (Lana et al., 2012). DMSPt is defined as the sum of

294    $DMSP_{dissolved}$ and $DMSP_{particulate}$ concentration. Yet, the amount of DMSPt per unit

295   phytoplankton biomass may vary depending on species composition and physiological state,

296   (Keller et al., 1989).

297   The dissolved organic carbon (DOC) concentrations in surface waters of the high Arctic

298   Ocean are up to ten times higher than in any other ocean basin and closer in range to DOC

299   levels reported for sea ice (Gao et al., 2012). A large fraction of DOC spontaneously

300   assembles into polymer gels: polysaccharide forming hydrated calcium bonded three-

301   dimensional networks to which other organic compounds, such as proteins and lipids, are

302   readily bound. The assembly and dispersion of the polysaccharide molecules can be affected

303   by environmental parameters, such as UV-B radiation (280-320nm) dispersing or inhibiting

304   gel formation, and/or pH and temperature inducing gel volume phase changes (swelling and

305   shrinkage). In the study of Orellana et al., (2011b), the swelling and shrinking of the

306   polysaccharide networks or polymer gels were also causally related by additions of nano to

307   micromolar levels of DMS and DMSP. High DMSP concentrations have also been measured

308   in the mucilage surrounding prymnesiophyte *Phaeocystis pouchetii* colonies in Arctic waters,

309   representing up to 25% of the total water column DMSP pool, (Matrai and Vernet, 1997).

310   The findings made by Orellana et al., (2011b) were in agreement with previous findings by

311   Orellana et al., (2011a) that high concentrations of DMSP and DMS are stored in the acidic

312   secretory vesicles of the *Phaeocystis* algae where DMSP is trapped within the condensed

313   polyanionic gel matrix until the secretory vesicles are triggered by environmental factors such

314   as temperature to release gels that undergo volume phase transition and expand at the higher

315   pH of seawater.   Exocytosis of polymer gels accompanied by elevated DMS and DMSP

316   concentrations suggests the transport of these chemical compounds by the gel matrix.

317   Schoemann et al., (2005) report that *Phaeocystis antarctica* is particularly well adapted to low

318   temperatures, being more competitive than *P. pouchetii for temperatures between -2* and

319   +2 °C. *Phaeocystis pouchetii*, however, appears to be better adapted to temperatures closer to

320   5 °C. In the Arctic a higher occurrence of the *Phaeocystis pouchetii* would be expected in the

321   northward advection of warm Atlantic water masses around Svalbard.

322   Here we estimated DMSPt at the sea surface using the algorithm described by Galí et al.

323   (2015). The DMSPt algorithm exploits the distinct relationship between DMSPt and

324   Chlorophyll-*a* depending on the light exposure regime of the phytoplankton community. The

325   light exposure regime is defined by the ratio between euphotic layer depth and mixed layer

326   depth (Z_{eu}/MLD). Additional predictor variables used are sea surface temperature (SST) and

327   particulate inorganic carbon (PIC), which is used in the algorithm as a proxy for

328   coccolitophores such as *Emiliania huxleyi*. During late bloom stages, the calcite plates that

329   cover coccolitophore cells (called coccoliths) detach and cause an increase in seawater

330   backscatter that invalidates satellite retrievals of Chlorophyll-*a*. Therefore, inclusion of PIC

331   in the algorithm as a proxy for DMSPt increases data coverage. Although the algorithm was

332   developed for the global ocean, validation results with in situ data indicate that it performs as

333   well or slightly better in Arctic and sub-Arctic waters.

334   The use of remotely sensed DMSPt as a proxy for marine DMSaq emission is a significant

335   improvement with respect to prior studies that used Chlorophyll-*a* (Becagli et al., 2016;

336   Zhang et al., 2015). Yet, it is not ideal because (i) the ratios DMS_{aq}/DMSPt in surface

337   seawater are variable, and tend to be higher in high solar irradiance and nutrient-poor

338   conditions typical of summer, (Galí and Simó, 2015), and (ii) even if DMSPt is a better proxy

339   for DMS_{aq}, the influence of meteorological and sea surface conditions (mainly wind speed

340   and SST) on the sea-air flux of DMS_{aq} is not taken into account. Development is underway of

341   an algorithm for the retrieval of DMS_g concentrations in air and DMS fluxes.

342   The DMSPt algorithm was run for the 2006-2015 period using daily composites of the

343   Moderate Resolution Imaging Spectroradiometer on the Aqua satellite (MODIS-Aqua) at 4.64

344   km resolution (L3BIN, reprocessing R2014.0) downloaded from NASA's Ocean Color

345   website (http://oceancolor.gsfc.nasa.gov). The MODIS variables used include Chlorophyll-*a*

346   concentration derived with the GSM algorithm, (Maritorena et al., 2002), PIC, nighttime SST

347   and Z_{eu}. MODIS nighttime SST was complemented with SST from the Advanced Very High

348   Resolution Radiometer (AVHRR, https://podaac.jpl.nasa.gov/AVHRR-Pathfinder) to increase

349   data availability. MLD was obtained from the MIMOC climatology, (Schmidtko et al.,

350   2013), which was linearly interpolated from its original 0.5°x0.5° grid at monthly resolution

351   to the MODIS grid at daily resolution.

352   Satellite remote sensing of biological activity in surface waters requires ice-free and at

353   least part of the time cloud-free. The passive sensing methods of MODIS additionally require

354   a minimum of solar illumination of the scenes (i.e., solar zenith angle < 70°; (IOCCG, 2015)).

355   Consequently, the length of the satellite-observable period used to compute DMSPt means

356   shortens from all-year-round at latitudes <45° to approximately six months (the spring-

357   summer semester) at 80°N. In addition, the annual DMSPt map in Fig. 3 excludes all land and

358   ice covered regions. In order to increase data coverage, daily DMSPt composites were binned

359   to five-day periods and a 46.4 km equal-area sinusoidal grid, (10x10 bins of the original pixel

360 size). The average distance between a trajectory point and the closest center of a MODIS

361 pixel is 18 km.

362 Following the same approach as with the ice data average DMSPt from ocean color data,

363 (OC), along each back trajectory were calculated and will be referred to as OC1 (the last day),

364 OC2 (the last but one day), and OC5 (days three to five) before arrival at Mt. Zeppelin. In

365 this procedure missing data were flagged as such, and were not taken into account.

366

367

368 **2.5   Ice data**

369

370 For the interpretation of events of new particle formation observed during the *Oden* cruises

371 information on pack ice extent under the air masses reaching the sampling points proved

372 crucial (Heintzenberg et al., 2015). Another motivation for utilizing ice data in the present

373 study is the fact that the Svalbard region experiences large seasonal changes in pack ice cover

374 which we expect to have strong effects on emissions of particles and their precursor gases.

375 Thus daily sea ice concentrations from Nimbus-7 SMMR and DMSP SSM/I-SSMIS passive

376 microwave data were taken from the NSIDC database (https://nsidc.org/data). The irregularly

377 shaped data gap around the pole caused by the inclination of satellite orbits and instrument

378 swath was filled with 100% cover. To each hourly position and data of the back trajectories

379 the ice information in the corresponding maps of ice concentrations were added and displayed

380 in Fig. 2. On average the closest pixel in the ice maps was about 12 km off any trajectory

381 point.

382 In the discussion of results we utilize the complement of ice cover, i.e., the amount of open

383 water because the marine biological processes of interest predominantly take place in the

384 open water, (Leck and Persson, 1996a). As integral parameters average open water, (OW),

385 percentages along each back trajectory were calculated and will be referred to as OW1 (the

386   last day*)*, OW2 (the last but one day), and OW5 (days three to five) before arrival at Mt.

387   Zeppelin. The most solid ice cover is seen in an area reaching from Northeastern edge of

388   Greenland via North Pole to Parry Island. A marginal ice zone extends along the east coast of

389   Greenland to Franz-Josef-Land, and the area between Svalbard and the latter island.

390

391

392   **2.6   ERA-Interim data of sea surface temperature**

393

394   Daily Sea Surface Temperature (SST) data for our study period (2006-2015) were

395   downloaded from the website of the European Centre for Medium-Range Weather Forecasts

396   (ECMWF). A description of the global atmospheric reanalysis, (ERA-Interim), has been

397   given by Dee et al. (2011), and a guide to the products and the download procedures can be

398   found at http://www.ecmwf.int/en/elibrary/8174-era-interim-archive-version-20. Briefly,

399   ERA-Interim is an assimilating model reanalysis of the global atmosphere and sea-surface

400   physical parameters covering the data-rich period since 1979. SST data were downloaded at a

401   resolution of approximately 0.56° and regridded onto the same 46 km equal-area sinusoidal

402   grid used for DMSP and cloud fraction, (see below). Ice-covered pixels were screened out

403   prior to the back-trajectory analysis. In the Arctic region, ERA-Interim has been shown to be

404   a top performer among a number of atmospheric reanalyses, (Lindsay et al., 2014).

405

406

407   **2.7   MODIS cloud fraction**

408

409   Persistent cloud cover limits PPP in Arctic and Sub-arctic seas, (Bélanger et al., 2013), and,

410   as mentioned above, irradiance at the sea surface, which is largely controlled by cloudiness,

411   influences $DMSP_{dissolved}$-to-DMS_{aq} conversion. Boundary layer clouds are known to be

412   additional controllers of the surface aerosol (Heintzenberg, 2012). In the summer Arctic low

413   level clouds and fogs are widespread (Warren and Hahn, 2002). Both scavenging and new

414   particle formation have been observed in connection with low clouds and fog passages

415   (Lannefors et al., 1983; Heintzenberg and Leck, 1994; Leck and Bigg, 1999; Heintzenberg et

416   al., 2006; Karl et al., 2013). Beyond the cloud base derived from the ceilometer we have no

417   other in situ local or regional cloud information. Thus, we utilize satellite-derived cloud

418   information.

419   Daily Level-3 global cloud fraction with one-degree resolution was downloaded from

420   NASA website (http://modis-atmos.gsfc.nasa.gov, Hubanks et al., 2015) and extracted for our

421   region of interest. Briefly, level 3 images correspond to the aggregation of all level 2 images

422   (1 km resolution) available within the one-degree resolution grid. For a given L2 scene, each

423   pixel is assigned a value of 1 (cloudy) or zero (clear sky), and then the individual scene values

424   are averaged over a 24-hour period. Note that a given pixel can be revisited up to six or seven

425   times in the course of a day at high latitudes. Finally, the daily composites were re-projected

426   to 46.4 km pixels to match the spatial resolution of DMSPt. The average distance between a

427   trajectory point and the closest MODIS pixel was 18 km.

428   The cloud fraction CF as well as other cloud properties from MODIS have been

429   extensively used, for instance to study the global spatial and temporal distribution of clouds

430   over the last decade (e.g., King et al., 2013). Several studies have also successfully

431   performed validation by comparison with in situ data (e.g., An and Wang, 2015) which

432   demonstrated the ability of the MODIS-aqua sensor to retrieve cloud cover.

433   Following the same approach as with the ice data and DMSPt, average cloud fractions,

434   (CF, see Table 1), along each back trajectory were calculated and will be referred to as CF1

435   (the last day), CF2 (the last but one day), and CF5 (days three to five) before arrival at Mt.

436   Zeppelin. Missing data are flagged as was done with DMSPt data.

437

438

3. Three approaches to identifying events of new particle formation

440

There are no definitive and no generally accepted methods to identify or predict NPF-events in atmospheric time series of aerosol data. Thus, in the present study we explored different approaches with varying degrees of complexity to identify such events. We emphasize that none of these approaches explicitly is connected to diel cycles such as in Dal Maso et al., (2005) or makes any assumptions about the time of day during which new particle formation occurs. Three objective search algorithms were written in FORTRAN to analyze the time series of hourly records of aerosol parameters in search of new particle formation:

1. The simplest approach of upper percentiles (PCT-approach), assumes that NPF-events are characterized by extremely high concentrations of small particles in terms of N25 (see Table 1). The key parameter characterizing each PCT-event was the value of N25 averaged over a fixed number of hours, (N25$_{av}$), after the nominal start of an event, (see below). With N25$_{av}$ also a nominal length of PCT-events was defined as the number of hours after the start of an event by which N25 sank to less than half of N25$_{av}$.

2. The more specific approach of diameter growth (DGR-approach) builds on the temporal development of the particle size distribution in terms of a systematic growth of the diameter D50 (see section 4.1) to find the classical "Banana Type" of NPF-event, (Kulmala et al., 2004). The key parameter characterizing each DGR-event was the average growth of D50 during the nominal event length NUC, (see below). For this approach the nominal length of events was reached when the running two-hour average growth fell below the value one.

2. The most complex approach of multiple-size events, (MEV-approach), searches for events with concurrent appearance of concentration increases in several size classes below 60 nm diameter (Karl et al., 2013; Leck and Bigg, 2010). The key parameter characterizing each

464   MEV-event was the relative concentration increase averaged over the chosen size classes

465   below 60 nm during the nominal event length NUC, (see below). As with PCT-events a

466   nominal length of MEV-events was defined as the number of hours after the start of an

467   event by which N25 sank to less than half of $N25_{av}$.

468

469   Three time-related parameters were commonly defined for all three approaches:

470   1. Nominal NPF-event length, (NUC) was nine hours.

471   2. Pre-event periods, (PRENUC), from which increases in diameters or number

472   concentrations were calculated, were six hours.

473   3. Reference periods, (REF), before PRENUC and after NUC periods were defined in order

474   to compare event and pre-event data with non-event conditions. Each of these reference

475   periods had the length of half the sum of pre-event plus event time periods, making the

476   total reference time period of each event as long as that of the event itself.

477   Besides these common characteristic lengths individual fixed thresholds were chosen and

478   discussed below for each approach in order to generate at least 200 unique events per

479   approach, (see Table 2).

480   The aerosol data used to define the NPF-events were complemented by a large number of

481   environmental parameters. The primary temporal resolution of the environmental parameters

482   was between one minute (C25, cf. Table 1) and five days (DMSPt, cf. Table 1). C25 was

483   calculated as 25% percentile on an hourly basis. The parameters with resolutions higher than

484   an hour (OW, CF, and OC, cf. Table 1) were evaluated along the hourly back trajectories.

485   While this procedure yielded hourly varying results even of OW, CF, and OC it has to be kept

486   in mind that this hourly variability is the result of hourly resolved trajectories traversing the

487   grid; the low primary temporal resolutions of the OW, CF, OC, and chemical parameters

488   remain. For these slowly varying parameters the REF periods before and after the events

489   were extended to one day beyond the longest primary resolution, i.e., six days.

490   For two reasons the three search algorithms may yield temporarily redundant results, i.e.,

491   they may identify the same events. One, they go independently through the same time series

492   of aerosol data, possibly causing inter-approach redundancy. Two, each algorithm goes

493   through the time series hour by hour, thus allowing for temporal overlap of events found by

494   each approach, (intra-approach redundancy).

495   The three types of events were assumed to be mutually exclusive and potentially being

496   caused by different sets of conditions for new particle formation. Thus, a FORTRAN

497   procedure was developed to eliminate both intra and inter-approach redundancy while

498   maintaining a maximum of identified NPF-events. To remove intra-approach redundancy the

499   procedure identifies overlapping events within each approach. Of each ensemble of such

500   overlapping events the one with the strongest key parameter of the respective approach

501   (growth of D50, or concentration increases as defined above) is retained. Next, inter-

502   approach redundancy is addressed by the procedure. However, there is no unique solution to

503   the problem of the partly redundant three time series of events. In order to avoid any

504   preference of one or several types of events in the tests of inter-approach overlap pairs of

505   events of different approaches are chosen at random and compared for overlap. This random

506   comparison is done as often as the product of the number of events of the three approaches.

507   This rather time-consuming random test yields stable numbers of non-overlapping events

508   within less than one percent, irrespective of the order in which the events of the three

509   approaches were arranged for the test. By removing intra and inter-approach redundancy in

510   the first two steps of the procedure a number of time periods will be "freed". Consequently,

511   in a last step, the procedure tries to fill the "freed time periods" non-redundantly with events

512   of the three approaches that had been eliminated in the first two steps. Table 2 collects total

513   numbers and unique numbers of events for each approach. In the rest of the paper only non-

514   redundant events will be discussed. The total number of new particle formation events will

515   be shortened to TNPF.

3.1 The upper percentile of N25 (PCT-approach)

Events of new particle formation were identified by time periods in which N25 was consistently, i.e. on average for three hours, above a set threshold. With a threshold of the 93%-percentile (170 cm^{-3}) 4143 PCT-events were identified in the total data set, only 240 of which were unique because most of them overlapped with event or pre-event times of the other two approaches. Average N25 during these unique events was 330 cm^{-3} and the average length of events 4 ±0.9 h, (one standard deviation).

Fig. 4, (top), shows the average temporal development of the relative size distributions for the unique PCT-events as in the results in Karl et al. (2013), i.e. relative concentrations were formed by dividing the absolute number concentrations by the average total number during the six-hour pre-event time periods. The events are characterized by a nearly monomodal distribution around 20 nm that broadens somewhat around the nominal start of the events. During the last three hours before the events D50 decreased slightly and returned to the pre-event level during the nine NUC hours.

In connection with PCT-events average aerosol parameters NTO through N300 showed an average increase by a factor of 2.2 during PRENUC-periods, which was maintained on an average level of 1.5 during the events. The aerosol-chemical parameters Na^{+}, nssSO$_4^{-2}$, and MSA were on an average level of 20% of their reference value. The average environmental parameters indicate a strong increase by a factor of 14 in solar radiation and a lifting of cloud base before the events. During the events the level of solar radiation was still elevated by a factor of six above its reference value. As a consequence temperature at the station was up by 2 – 3 degrees. Precipitation 12 h before trajectory arrival time, (SP12) was a factor of five above reference levels for air arriving during NUC-periods, whereas SP35 to SP5D were below their respective reference levels. Cloud fractions were slightly raised 12 - 48 h before air arrival. Of the ocean parameters more open water was met by trajectories 12 to 24 before

542   their arrival with ocean temperatures 12 to 48 h before trajectory arrival having been up to

543   four degrees warmer than their respective reference values. On average DMSPt-parameters

544   OC24 through OC5D showed were raised by a factor of two above their reference value.

545   In Fig. 5, (left top panel), average trajectory height profiles during PRENUC and NUC-

546   periods are displayed. Widely varying vertical air mass paths occurred before and during

547   PCT-events. Median vertical trajectory paths during PRENUC and NUC times indicated air

548   coming from some 300 m above station level five days ago sinking to about one hundred

549   meters above station level during the last two days before arrival. The upper quartiles of the

550   PCT-height profiles point at strong subsidence before air mass arrival.

551   The right top panel in Fig. 5 maps average horizontal trajectory positions in 12 h steps in

552   months having at least ten PCT-events, i.e., May - September. Filled circles around the

553   trajectory positions comprise 95% of all events. The monthly average horizontal trajectory

554   direction during PCT-events mostly was from the northwest. In June and July the trajectories

555   reached farthest into the multiyear ice cover northeast of Greenland. Only during September

556   the back trajectories covered ice-free and marginal ice areas in the Fram Strait. We note that

557   the five-day back trajectories of PCT-events, (and of the other two approaches as well), stayed

558   within some 800 km of Mt. Zeppelin.

559

560

561   **3.2   The diameter growth (DGR) approach**

562

563   The DGR-approach to identify events of new particle formation builds on the classical

564   concept of particle growth through condensable vapors after an initial nucleation of sub-five

565   nanometer particles that cannot be observed with the available instrumentation, so called

566   "Banana-type" (Kulmala et al., 2004). The respective algorithm utilizes the parameter D50,

567   (see Table 1), and requires a growth of this diameter by at least a factor of 1.5 after the

568 nominal start of an event. With this threshold the algorithm searched through all 87646 hours

569 of the ten-year record and found 1199 DGR-events of new particle formation. After

570 eliminating cases of temporal overlap with the other two approaches 235 unique events of this

571 type remained, (see Table 2). Other or more DGR-events could have been found by

572 shortening the nominal nine NUC hours. For two reasons we refrained from discussing

573 shorter growth periods in the DGR-approach. Maintaining common-length NUC periods

574 facilitated the comparison of results of the three approaches. Furthermore, reducing the

575 growth period would also make PCT and DGR-events ever more similar.

576   In the analysis of atmospheric data and theoretical modeling of NPF-events of type DGR

577 two key parameters are discussed, namely particle formation rate J ($cm^{-3}s^{-1}$) and growth rate

578 GR (nmh^{-1}) of particle diameters. For both parameters the measurement protocol by Kulmala

579 et al. (2012) provides specific calculation procedures, (equations. 2, 7, and 9), which we

580 follow in the present study, albeit with the caveat that the one-hour temporal resolution of our

581 time series is far below the ten-minute time resolution that the protocol of Kulmala et al.

582 (2012) requests in order to be able to follow the rapid development of NPF-events.

583 Furthermore, only the 127 DGR-events identified from 2011 on are based on particle size

584 distributions measured down to a diameter of five nanometers.

585   The sizes of newly nucleated aerosol particles are of order 1–2 nm, which is below or near

586 the limit of existing measurement techniques. When the nuclei grow in size their number

587 concentration decreases because of various removal mechanisms. Instead of particle

588 formation rates at the initial nucleus size so-called apparent nucleation rates Jx are often

589 reported, i.e. rates at which new particles appear at some larger observable particle diameter

590 dx. For the present study two apparent nucleation rates are calculated: DGR events of the

591 whole time series have been identified with particle size distributions measured at diameters

592 from 10 nm up through the growth of the number median diameter D50 in the size range 10 –

593   50 nm. Thus we calculated J22 for these 235 events at the nominal geometric mean diameter

594   of 22 nm. For 127 of these events size distributions reached down to five nanometer

595   diameter, (years 2011 and later). For these events we calculated J11 at the geometric mean

596   diameter 11 nm as representative for the diameter range $5 - 25$ nm, which is close to the

597   frequently reported apparent formation rate J10 at 10 nm diameter. Additionally, the two

598   corresponding grow rates GR22 and GR11 were calculated in the respective diameter ranges.

599   Statistics of these four key parameters of the DGR events are collected in Table 3.

600   Depending on the pollution level at the measuring site widely varying values of J10 have been

601   reported. For the polluted subtropical environment of Taiwan Young et al. (2013) give values

602   from 4.4 to 30 $cm^{-3}s^{-1}$ whereas Pierce et al. (2014) published values between 0.22 and 0.84

603    $cm^{-3}s^{-1}$ from a rural Canadian setting. The latter range is within the range $0.1 - 9.4$ $cm^{-3}s^{-1}$

604   with a median value of 1.2 $cm^{-3}s^{-1}$ reported by Yli-Juuti et al. (2009) for a station in rural

605   Hungary. The two formation rates of the present study cover the range $0.1 - 1.4$ $cm^{-3}s^{-1}$ for

606   the 25% to 75% percentiles (see Table 3), which covers the range of 0.05 to 0.13 $cm^{-3}s^{-1}$ given

607   by Vencaz et al. (2009) for a remote site in the Himalaya. The environmental conditions at

608   the Siberian station Tiksi at the coast of the Laptev Sea may come closest to our Arctic

609   setting. From this site Asmi et al. (2016) published formation rates of 0.01 to 0.41 at an

610   unspecified particle size.

611   In terms of 25% to 75% percentiles the particle growth rates of the present study range

612   from 0.4 to 1.4 nmh^{-1} in the range $5 - 25$ nm and 1.0 to 1.8 nmh^{-1} in the diameter range 10 -

613   50 nm, which is near the range of results of $1 - 2$ nmh^{-1} derived by Ström et al. (2009) for

614   new particle formation in the lower boundary over Ny-Ålesund, Spitsbergen but considerably

615   lower than the maximum growth rate of 3.6 nmh^{-1} reported by Asmi et al. (2016) for July at

616   the Siberian station Tiksi at the coast of the Laptev Sea. For open ocean new particle

617   formation events over the North Atlantic O'Dowd at al. (2010) report a "typical growth rate"

618   of 0.8 $nmh^{-1,}$ whereas Ehn et al. (2010) give an average growth rate of 3 nmh^{-1}. We note that

619   the average length of DGR-events was 10 ± 1 h, (one standard deviation). Further details

620 about the connection between growth rates and the two formation rates can be found in the

621 supplement.

622   The average temporal development of the relative number size distribution during DGR-

623 events is presented in Fig. 4, (center). After a decrease of the sub-50 nm diameter median

624 from about 25 to 16 nm during the six hours before the nominal start of the events D50

625 increases systematically during the following nine NUC hours with somewhat reduced growth

626 towards the end of the event.

627   During the PRENUC-periods particle number concentrations N300, and the condensation

628 sink, (CS), decreased relative to the reference periods before and after the events.

629 Subsequently, during the NUC periods the strongest increases was found for N60.

630 Environmental parameters around air mass arrival showed a strong lifting of cloud base,

631 (C25), and an extremely high increase in solar radiation, (by a factor of 11 during PRENUC

632 and by a factor of 60 during NUC periods). However, 12 h before air arrival precipitation had

633 been up by a factor of 2.5. Cloud fractions were down to about 70% of their reference values

634 24through 48 h before air arrival. Of the chemical aerosol parameters Na^+ and $nssSO_4^{-2}$

635 showed an increase of 2.6 and 2.3, respectively. OC12 and OC48 were slightly higher than

636 reference level before and during the events. Sea surface temperatures T24 were raised by

637 nearly one degree whereas earlier SST-values, (T36 – T5D), were up to one degree below

638 reference values.

639   Fig. 5, (left center panel), shows statistics of the vertical air movement before trajectory

640 arrival during DGR-events at Mt. Zeppelin covering a wide range of vertical movements

641 between 200 m and beyond 1500 m height. During the days when elevated DMSPt levels

642 were noted median trajectory heights were six to nine hundred meters. Median trajectories

643 during PRENUC times dipped down to the station level, (474 m a.s.l), about one day before

644 arrival, albeit lifted and subsided again shortly before arrival. Vertical trajectory pathways

645 will be discussed further in Section 4.2.

646   Monthly average trajectory positions and their variability in connection with DGR-events

647   are shown in Fig. 5, (center right panel). The months April through October had at least ten

648   DGR-events per month. As with PCT-events the general trajectory direction was from the

649   northwest, mostly staying for several days over the marginal ice zone between northeastern

650   Greenland and eastern Svalbard. During the earliest month of April with 14 DGR-events the

651   back trajectories reached farthest south into the ice-free parts of the Fram Strait.

652

653

654   **3.3   The Multiple-size approach (MEV)**

655

656   Leck and Bigg (2010) and Karl et al. (2013; 2012) discussed a type of new particle formation

657   that to date only has been reported from the summer Arctic. During these MEV-events high

658   ultrafine particle concentrations appear concurrently in a broad diameter range reaching from

659   under 10 to some 60 nm. We simulated this type in a search that required the concurrent

660   increase of NTO, N20, N40, and N60, (cf. Table 1), as averaged over the first three NUC

661   hours by a factor ≥ 1.6 over their respective averages during the six (PRENUC) hours. Over

662   the ten years of data 1191 such events of this type were identified, 266 of which remained

663   after removal of those overlapping with events of other approaches. During these unique

664   events the average concurrent concentration increase was 4.7 and the average length of the

665   events 12±0.8 h.

666   The concurrent appearance of high concentrations at many particle sizes below 60 nm

667   resembles the nocturnal NPF-events analyzed by Suni et al. (2008) in the Australian

668   Eucalyptus forest and simulated in subsequent chamber experiments (Ristovski et al., 2010;

669   Junninen et al., 2008). We emphasize though that the condensing vapors in the Australian

670   NPF-events originating from terrestrial biogenic emission are quite different from the

671 polymer gels implicated in the Arctic MEV-events and originating from the surface

672 microlayer of the ocean.

673 The bottom part of Fig. 4 shows the average temporal development of relative number size

674 distributions before and during MEV-events. The development before the nominal start of

675 MEV-events is more complex than during the PRENUC-periods of the first two types of

676 events. Intermittently a mode around seven nanometers shows up that broadens and becomes

677 more prominent about two hours before the nominal start of events. The major PRENUC-

678 mode around 25 nm also broadens and becomes more prominent towards NUC. A weak

679 mode exists during PRENUC around 120 nm and hardly any particles beyond 400 nm. D50

680 sinks from 25 to about 20 nm and stays below 25 nm through the MEV-events even though

681 number concentrations increase during the first NUC-hours by more than a factor of five.

682 During NUC-periods all particle number concentrations increased, on average by a factor

683 of 1.6. Average solar radiation also increased by about 90% above reference level during

684 NUC-periods. Of the chemical parameters $nssSO_4^{-2}$ showed an increase by a factor of three

685 during PRENUC and NUC-periods, and MSA a slight increase during PRENUC-periods. On

686 one hand, precipitation 12 h, and 36 to 48 h before trajectory arrival, (SP12, SP48), were

687 above reference levels for air arriving during PRENUC-periods. On the other hand, during

688 PRE, SP24, SP36, an SP5D indicated dry conditions during PRENUC and NUC-periods.

689 Only three to five days before air arrival slightly increased cloud fractions were noted. Sea

690 surface temperatures up to five days before trajectory arrival were on average about one

691 degree lower than their reference values. DMSPt parameters OC12 to OC36 were raised by

692 factors of 1.3 and 1.6 during PRENUC and NUC-periods, respectively.

693 Percentiles of vertical trajectory coordinates prior to and during MEV-events are displayed

694 in Fig. 5, (bottom left panel). During the events, and even stronger during the PRENUC

695 periods median trajectories had been below 500 m for more than four days. Furthermore, the

696 final air approach to Mt. Zeppelin mostly came from below the station level. Upper quartiles

697   of the vertical trajectory positions are substantially lower than with DGR-events. We note,

698   however, that a short excursion above station level occurred in the upper quartiles during the

699   last three hours before arrival.

700   The bottom right panel of Fig. 5 gives the monthly average trajectory positions and their

701   variability in connection with MEV-events. The months April through October had at least

702   ten MEV-events per month. As with the other approaches the general trajectory direction was

703   from the northwest, albeit with stronger swings towards the ice-free areas south of Svalbard

704   early and late in the season, (April, May, and September). Interestingly, the trajectories of the

705   11 MEV-events in October were directed nearly straight north from the North Pole.

706   Summarizing differences and commonalities among the results of the three approaches we

707   can state that the length of the events increases from four to ten and twelve, going from PCT

708   to MEV-events. PCT-events are characterized by lower-than-reference aerosol-chemical

709   parameters. Na^+ and $nssSO_4^{-2}$ show strong increases in the other two types of events: Na^+ in

710   connection with DGR-events and $nssSO_4^{-2}$ in connection with MEV-events. Both, PCT and

711   DGR-events exhibit strong increases in solar radiation. Precipitation before air arrival was

712   raised at varying times in connection with the three types of events. Cloudiness both

713   increased and decreased at varying times before air arrival with the three types of events.

714   Increased open water under the trajectories was strongest with DGR-events and least

715   important with MEV-events. Only in connection with PCT-events strongly raised sea surface

716   temperature were noted before trajectory arrival. DMSPt related ocean parameters were

717   raised to varying degrees and at varying times before all NPF-events, most strongly in

718   connection with PCT-events and least in connection with DGR-events.

719

720

721   **4. Discussion**

722

4.1. Environmental setting

The discussion of the results on new particle formation in the Svalbard region builds on the variability of new particle formation and related environmental parameters on scales of months, and days. Fig. 1 gives an overview over the geographic areas which were covered by one, two, and five-day back trajectories to Mt. Zeppelin during the ten years of the present study covering the months March through October. This figure illustrates that air arriving at Mt. Zeppelin during the ten summers of the present study came from widely varying regions from the central ice-covered Arctic via the northern seas and northernmost Scandinavia to Greenland. One-day back trajectories cover a roundish area from the central east coast of Greenland via northern Scandinavia to Franz-Josef-Land, North Pole and back to the north coast of Greenland. Excluding inner Greenland this area is widened by roughly 500 km by 2-day back trajectories and by at least another 500 km by 5-day back trajectories reaching over most of Greenland and the adjacent seas west of Greenland. This is a much wider region from which air may reach Mt. Zeppelin as compared to sites in the inner Arctic as illustrated in Fig. 2 of Heintzenberg et al. (2015).

On the path of trajectories to Mt. Zeppelin quite different ice conditions were met (see, Fig. 2). On average North Atlantic open waters reached around West Spitsbergen all the way to Nordaustlandet. Drift ice was passed over by trajectories along the whole east coast of Greenland. One-day trajectories passed over the marginal ice zone from the Fram Strait to Franz-Josef Land but also over more contiguous ice close to the North Pole. At times, with five-day back trajectories, even the marginal ice regions of Baffin Bay and Beaufort Sea were reached.

The long-term geographical distribution of DMSPt in Fig. 3 reflects the water conditions for phytoplankton biomass around Svalbard. Directly at the coasts of Greenland and Eurasia increased nutrient availability in coastal and shelf waters (due to continental run-off and

749 enhanced hydrodynamics) cause localized areas of high DMSPt values. The low DMSPt

750 values further out along the coast of Greenland are due to sea ice reaching through the Fram

751 Strait far south, (see Fig. 2). A prominent feature in the regional DMSPt distribution is the

752 tongue of high DMSPt, (intense blue color), and thus high phytoplankton biomass east of this

753 area, reaching from Spitsbergen to roughly Jan Mayen that lies within one-day back

754 trajectories. Northward-flowing Atlantic waters, carried by the West Spitsbergen Current,

755 and southward-flowing fresh surface waters from melting ice, and recirculated Atlantic

756 waters, carried by the East Greenland Current (Rudels et al., 2005) are meeting. The layering

757 created by water masses of different density stabilizes the water column and traps

758 phytoplankton cells at well-lit depths. If sufficient nutrients are available, this can lead to the

759 development of large phytoplankton blooms, which can result in high concentrations of

760 DMS$_{aq}$, (see Fig. 2 in Leck and Persson, 1996a).

761 In the ten-year average cloud fractions systematic differences in cloudiness appear.

762 Depending on transport pathways as identified by the back trajectories, cloudiness varies on

763 the way to Spitsbergen. The ice-covered areas, (cf. Fig. 2), from the east coast of Greenland

764 to Franz-Josef-Land exhibit somewhat lower cloud fractions than the ice-free regions

765 southwest to east of Spitsbergen.

766

767

768 **4.2 Seasonal variability**

769

770 Seasonal changes are discussed in terms of monthly averages taken over the ten-year study

771 period. As expected in Earth's polar regions the seasonal variability of all environmental

772 parameters is very high as exemplified by the solar flux, (SFL), and the air temperature,

773 (TEM), at Mt. Zeppelin in Fig. 6. Due to the seasonal change in cloudiness, (cf. Fig. 7), the

774 seasonal distribution of SFL is not quite symmetrical about midsummer but is skewed slightly

775   towards the cloud minimum in spring. The air temperature, however, does not peak before

776   July and has a broad shoulder into fall and winter. The first, and partly absolute maxima, of

777   the seasonal distributions of NPF-events in Fig. 6 coincide with that of the SFL but then drop

778   of more slowly towards fall than solar radiation. In particular, MEV-events do so and even

779   have their main maximum in August. The occurrence of all NPF-events drops off sharply in

780   October. Whereas May as the first month with larger numbers of events is dominated by

781   PCT-events, followed by DGR and then MEV-events, the contributions of the three NPF-

782   types are reversed in the last month with high NPF-numbers, i.e., September.

783   Fig. 6 clearly shows that the formation of new particles in the Svalbard region is not

784   controlled by the late winter-to-early-spring phenomenon of Arctic haze peaking with highest

785   sulfate-concentrations in March, (cf. Fig. 3 in Heintzenberg, 1989, and Fig. 6), which has a

786   minimum in the total number of NPF-events. This minimum is in contrast with the maximum

787   in new particle formation rates found by Croft et al. (2016a) with their global aerosol model.

788   The high numbers of accumulation mode particles during the Arctic haze months in late

789   winter and spring yield the annual maximum in condensation sink, (CS in Fig. 6), which

790   could quench nucleation events and subsequent growth. Thus, even though photochemistry

791   may produce significant amounts of nucleating material, the freshly formed particles will not

792   grow to stable size before they are removed via either deposition or coagulation as discussed

793   by Tunved et al. (2013) and others. An alternative explanation of the late onset of NPF-

794   events in TNPF in spring lies in the marine biological processes not being activated nearby

795   during the Arctic haze period yet, (Heintzenberg and Leck, 1994).

796   Fig. 7 collects the seasonal variation of environmental parameters as averaged along the

797   back trajectories to Mt. Zeppelin. From their minimum in March-April open water conditions

798   improve until September, after which the pack ice extent under the trajectories rapidly

799   increases again. The widening open water areas are reflected in sea surface temperatures

800   under the trajectories that increase until September before they drop off strongly in October.

801   Consequently, because of its connection to marine biological activity DMSPt increases in the

802   euphotic zone from first photosynthetic light in May until it evens out around July and drops

803   off in October. Largest DMSPt values are reached in the vicinity of Svalbard, (cf. OC12 in

804   July and August in Fig. 7), i.e. considerably later than MSA. The ending of DMSPt-curves in

805   October is due to the lack of data not due to zero-DMSPt. Still, DMSPt concentrations are

806   expected to be low at this time of the year at temperate to polar latitudes due to low

807   phytoplankton biomass and low light exposure, (see Fig. 9 in Galí et al., 2015). In terms of

808   the MODIS-derived cloud fraction cloudiness increases rapidly from its minimum in April

809   and evens out on a plateau of $80 - 90\%$ after July. The spring-minimum in cloudiness is

810   confirmed by the maximum in cloud base as indicated by C25 in Fig. 7. This seasonal

811   distribution of cloudiness does not correspond to the classical picture of near-surface

812   cloudiness that exhibits near cloud-free conditions in winter and mostly overcast with Arctic

813   stratus and fogs during the summer months (Warren and Hahn, 2002; Huschke, 1969). We

814   explain the difference by the specific atmospheric pathways covered by the back trajectories

815   of the present study (cf. Fig. 1). Trajectory-averaged precipitation parameters (SP12-5D in

816   Fig. 7) have minima in the period April – May, from which they increase towards their

817   maxima in fall and winter.

818   The chemical aerosol information derived from the analyses of filters samples has a

819   relatively low temporal resolution of at least one day combined with frequent gaps of several

820   days in between samples. Thus, it cannot directly be related to the time periods of NPF-

821   events. The seasonal distribution of chemical tracers, however, yields important information

822   about new particle formation. Taken over the whole year $nssSO_4^{2-}$ in Fig. 6 is largely

823   anthropogenic, (Heintzenberg and Leck, 1994), and has its maximum during the peak of

824   Arctic haze in March and April and its minimum in August, which does not match any

825   seasonal distribution of NPF-events. We also plotted Na^+ in Fig. 6 as a tracer of the inorganic

826   marine aerosol components sea salt. Na^+ decreases from its winter maximum to its summer

827   minimum in June/July, again without similarity to the NPF-distributions.   Instead, the

828   seasonal distribution of Na^+ rather closely follows that of the trajectory-derived wind speed

829   during the last hour before arrival, (not shown in the figure).   Wind speed as driver for sea salt

830   production is a well established phenomenon (Blanchard and Woodcock, 1957).   After a steep

831   rise in April MSA in Fig. 6 sharply peaks in May and then gradually drops off towards its

832   minimum in October, more gradually than reported for data taken from 1991 to 2004 by

833   Sharma et al. (2012) and earlier than reported by Heintzenberg and Leck (1994), both at the

834   same station.   Our seasonal distribution of MSA most closely resembles that of SFL, in Fig. 6,

835   albeit with its peak in May a month earlier that SFL and more strongly skewed towards

836   spring.   According to Leck and Persson (1996b) on average the concentrations of the marine

837   biogenic sulfur components, (DMS and MSA), fell with a decline rate of about 30% per week

838   approaching zero values in September explained by reduced ppp (Leck and Persson, (1996a),

839   (consistent with Becagli et al., 2016).

840   As MSA is the only measured aerosol component with exclusively marine biogenic

841   sources, we illustrate its seasonal distribution in greater detail in Fig. 8.   In this figure MSA-

842   concentrations measured on Mt. Zeppelin have been extrapolated along 5-day back

843   trajectories, forming monthly average monthly maps of potential MSA-sources during the

844   biologically most active months of March through October.

845   Fig. 8 yields several pieces of information that are relevant to the issue of new particle

846   formation.   Early in spring the biological aerosol sources are limited to the North Atlantic and

847   Norwegian Sea.   In April the tongue of newly opened waters between Novaya Zemlya and

848   Franz-Josef-Land seemingly is beginning to become biologically active.   In May this area

849   widens towards the Barents Sea while the North Atlantic also becomes more active, reaching

850   the Fram Strait.   In August two wide potential source regions cover the region from Northern

851   Greenland to the northern end of Scandinavia and the region Barents to Kara Sea.   In

852   September even the pack ice north of Svalbard becomes biologically active, (Leck and

853   Persson, 1996a), and shows potential MSA sources, in particular, north of the northern coast

854   of Greenland. Finally, the very weak potential MSA sources in October appear to be situated

855   mainly over the Kara Sea and over the North Atlantic.

856   How do these seasonal distributions compare to those of the NPF-events identified by the

857   three search-approaches defined in Section 3? To address this question we constrained the

858   average seasonal distribution of environmental parameters to those hours that had been

859   identified by the NPF-events of the three approaches. However, none of the individual

860   seasonal distributions of constrained environmental parameters follows closely any of the

861   NPF-events. In particular, the main MSA peak remains in May, thus one month earlier than

862   any peak of the NPF-occurrences. To elucidate further potential differences in the three types

863   of NPF-events we return to the discussion of vertical pathways of related back trajectories,

864   (see Fig. 5). In this figure all three types of NPF-events exhibit a wide range of vertical

865   trajectory paths. As we expect the regional sources of primary particles and particle

866   precursors to be at or near the surface we segregated the NPF-events into subpopulations with

867   back trajectories that remained a given time below 500 m, (roughly station level). In Fig. 9

868   we collected the results concerning the 93 NPF-events that occurred with trajectories under

869   the 500 m limit, i.e., roughly 12% of all events. The top panel shows that the related

870   trajectories not only stayed below 500 m through most of the last five days before arrival but

871   close to the surface until they started rising to the station level about 24 h before arrival. The

872   peak of the sum of event occurrences now coincided with the main MSA peak in May, (see

873   center panel in Fig. 9). For DGR-events the May-maximum was particularly strong whereas

874   the PCT-predominantly occurred in May and June and MEV-events remained clustered

875   around the later part of summer, possibly coupled to SST and DMSPt.

876   A number of environmental parameters indicated substantial deviations from their

877   respective reference values during the months with most frequent occurrence of this sub-

878   population of NPF-events. Strongest deviations were noted for precipitation that was elevated

above reference levels two to five days before trajectory arrival, most prominently for DGR-events in May, (by a factor of six 36 h before trajectory arrival). Strong positive deviations in aerosol-chemical parameters only occurred with Na^+ in PCT and MEV-events, indicating relatively high wind speeds near sea surface in the related air masses. MSA was elevated up to 50% above reference levels only during MEV-events. Elevated levels of DMSPt were noted with all three types of NPF-formation, most prominently for DGR-events 12 to 36 hours before which DMSPt was increased by a factor up to 1.7 relative to reference levels.

The bottom panel of Fig. 9 gives average trajectory positions in 12 h steps for the months May through September. The circles around the steps comprise 95% of all trajectories. During all months the trajectories stayed in the ice-free and marginal ice zone between Fram Strait and Eastern Svalbard as illustrated by average July ice cover for the ten study years, (for average monthly ice covers cf. Fig. 8). In particular during the earliest and latest months of May and September the trajectories swing farthest south over the open water south of Svalbard. We note that the complementary sub-population of results with trajectories remaining above station level did not yield results that differed strongly from those for the whole population of back trajectories.

As a last step in the discussion of seasonal variations in new particle formation a model is formulated that describes the average sum of NPF-events, (TNPF), as a function of three parameters, two of which are directly measurable at the site. With the linear combination of the solar flux, (SFL, Wm^{-2}), average sea surface temperature under back trajectories 36 to 48 hours before their arrival at the site, (T48, °C), and condensation sink, (CS, 10^5 s^{-1}):

$$TNPF = 0.57 \cdot SFL + 15.4 \cdot T48 - 0.69 \cdot CS$$

903   TNPF as shown in Fig. 10, can be described within an average deviation of 5% taken over the

904   major months with new particle formation, April - October.   Any other of the sea surface

905   parameters describes TNPF less satisfactorily.

906   **4.3   Diurnal variability**

907

908   Average hourly occurrence of the three types of NPF-events is plotted in Fig. 11, (top). The

909   three approaches yield rather similar diel variations. From their minimum during the night

910   and early morning hours they reach their maximum occurrence between 12 and 16 h UTC in

911   the afternoon. One might expect the differences between the NPF-types to be due to the

912   requirement of the three types of NPF formation being mutually exclusive. However, this

913   constraint does not exclude that they occur at the same time of day, only that they occur at the

914   same time on the same day.

915   Over the continents new particle formation and growth events of the classical "Banana-

916   type" usually exhibit an increase in measurable precursors such as sulfuric acid shortly after

917   sunrise followed by the detection of increased numbers of nanometer-sized particles between

918   one and two hours later (Kulmala et al., 2004), who deduce a connection to photochemically

919   produced condensable vapors from this daily pattern. In the Svalbard region the sun is up all

920   day between mid-April and the end of August. Consequently we would expect the

921   photochemical production of condensable vapors to have a smaller diurnal amplitude than at

922   lower latitudes, which in turn should even out the diurnal pattern of NPF-events to some

923   degree. Despite the relatively small daily variations in solar elevations the solar flux on Mt.

924   Zeppelin varied on average by more than a factor of five during the sunlit days (see curve

925   SFL in Fig. 11, bottom). The daily maximum of SFL between 12 and 15 UTC coincides well

926   with the average diel change in N25 and NPF-occurrence. As expected in particle growth due

927   to condensable vapors after initial nucleation the daily maximum in N10 precedes that of N25

928   by a few hours.

929   The other process controlling the development of newly formed small particles is the

930   diurnal development of the planetary boundary layer, (Kulmala et al., 2004). We have no

931   data on the daily variation in boundary layer structure over or near the measurement site. The

932   ceilometer data yield the only high-resolution information with some connection to the

933   structure of the planetary boundary layer. During the summer months these data show a

934   consistent daily variation with a jump in most frequent hourly cloud base by about 100 m

935   from about 1570 m after 09 UTC with rather stable values following until 16 UTC, after

936   which cloud base decreases again to values comparable to the early morning hours. The

937   hourly medians of the vertical displacement parameter DZ, (see Fig. 11, bottom), provide a

938   clearer diurnal variation. While being negative throughout the day, i.e. indicating subsiding

939   air during the last hour before arrival at Mt. Zeppelin, DZ indicates the weakest subsidence in

940   early afternoon. We interpret diurnal variation in cloud base and DZ as indicative of local

941   clearing and convection during the day that may be conducive to photochemical processes

942   and mixing in the boundary layer, both of which would be enhancing new particle formation.

943

944

945   **5. Summary and conclusions**

946

947   Three different types of events of new particle formation, (NPF), were identified through

948   objective search algorithms formulated for the present study. The first and simplest algorithm

949   utilizes short-term increases in particle concentrations below 25 nm, (PCT-events). The

950   second one builds on the growth of the sub-50 nm diameter-median, (DGR-events), and is

951   most closely related to the classical "banana-type" of events, (Kulmala et al., 2004) involving

952   the presence of photochemically generated DMS oxidation precursors. The third and most

953   complex, so-called multiple-size approach to identifying NPF-events builds on the hypothesis

954 of Leck and Bigg (2010), suggesting the concurrent production of polymer gel particles at

955 several sizes below about 60 nm, (MEV-events).

956   In this analysis the possibility that sporadic anthropogenic emissions were interpreted as

957 NPF events cannot be excluded completely. However, there are a number of facts arguing

958 strongly against this possibility leading to serious misinterpretation of the data:

959 a) Location and operation of the Mt. Zeppelin station exclude local contamination to a very

960 large extent.

961 b) Manual inspection of the time series by one of the co-authors (PT) further reduced the risk

962 of contaminated data.

963 c) The temporal evolution of MEV events, i.e. concurrent and sustained concentration

964 increases at several particle sizes below 60 nm does not correspond to a typical passage of

965 stack emissions from a large combustion source, (Ogren and Heintzenberg, 1990). Instead, it

966 looks very much like MEV events observed under even stricter constraints on local or

967 regional sources of contamination on icebreaker Oden in the central pack ice area, (Karl et al.,

968 2013), and also looks similar to nocturnal NPF-events in Australian forests, (Suni et al., 2008;

969 Junninen et al., 2008).

970   With these algorithms NPF-events were identified in a ten-year record of hourly number-

971 size distributions taken at the research station on Mt. Zeppelin, Spitsbergen. As a first and

972 general conclusion we can state that NPF-events are a summer phenomenon and not related to

973 Arctic haze, which is a late winter-to-early spring event. The seasonal distribution of the

974 available information on cloudiness does not suggest any direct connection with NPF-

975 formation. The MODIS derived cloud fraction generally is very high ($70 - 90\%$) and rather

976 evenly distributed over the Svalbard region during the months with high frequencies of NPF-

977 events. As already reported in Tunved et al. (2013) NPF-events appear to be somewhat

978 sensitive to the available data on precipitation derived from the trajectory model, in particular

979 when constrained to cases with back trajectories staying below 500 m. In this subpopulation

980 of NPF-events DGR-events show the strongest change in precipitation parameters in
981 connection with new particle formation.

982 The seasonal distribution of solar flux suggests some photochemical control that may
983 affect marine biological processes generating particle precursors and/or atmospheric
984 photochemical processes that generate condensable vapors from precursor gases. Whereas
985 the seasonal distribution of the biogenic MSA follows that of the solar flux it peaks before the
986 maxima in NPF-occurrence. For PCT-events, and more distinctly so for DGR-events, this
987 one-month delay disappears in the subpopulation with back trajectories staying below 500 m.
988 MEV-events, however, maintain their peak occurrence later in summer and early fall.

989 With the limited information on particle size, composition, particle precursors, and
990 environmental conditions no definitive statements can be made about the processes leading to
991 the formation of new particles in the Svalbard region. A host of findings, however, point to
992 varying and rather complex marine biological source processes. The potential source regions
993 for all types of new particle formation appear to be restricted to the marginal ice and open
994 water areas between Northeastern Greenland and Eastern Svalbard. During earliest and latest
995 months with high numbers of NPF-events the back trajectories reach farther south into the
996 open waters of the North Atlantic. Depending on conditions yet to be clarified new particle
997 formation may become visible as short bursts of particles around 20 nm, (PCT-events), longer
998 events involving condensation growth, (DGR-events), or extended events with elevated
999 concentrations of particles at several sizes below 100 nm, (MEV-events). The seasonal
1000 distribution of NPF-events peaks later than that of MSA and, DGR and in particular of MEV-
1001 events reach into late summer and early fall with much open, warm, and DMSPt-rich waters
1002 around Svalbard, promoting the production of *Phaeocystis pouchetii* together with polymer
1003 gels. Consequently, a simple model to describe the seasonal distribution of the total number
1004 of NPF-events can be based on solar flux, and sea surface temperature, representing
1005 environmental conditions for marine biological activity, and condensation sink, controlling

1006   the balance between new particle nucleation and their condensational growth. Based on the

1007   sparse knowledge about the seasonal cycle of gel-forming marine microorganisms and their

1008   controlling factors we hypothesize that the seasonal distribution of DGR and more so MEV-

1009   events reflect the seasonal cycle of the gel-forming phytoplankton.

1010   Despite the rather small diel changes expected during the summer Arctic there is a

1011   significant diurnal variation in aerosol and environmental parameters. Diurnal distributions

1012   of particle numbers below ten, (N10), and below 25 nm, (N25) follow that of the solar flux

1013   rather closely with a maximum between 14 and 16 UTC with the maximum of N10 occurring

1014   a few hours before that of N25. This delay in maxima may be caused by a slow particle

1015   growth due to photochemically produced condensable vapors. With a peak around noon

1016   MEV-events show the earliest daily peak occurrence with PCT and DGR-events peaking

1017   between 15 and 17 h, more closely to the maximum solar flux. Considering the diurnal

1018   variation in vertical trajectory displacement, (DZ), the early daily maximum in MEV-

1019   occurrence may be simply controlled by boundary layer dynamics.

1020   With the large database of ten years of aerosol data on Mt. Zeppelin enriched by

1021   environmental atmospheric and marine data occurrences, pathways and potential source areas

1022   of different types of new particle formation in the Svalbard region were elucidated by the

1023   present study. More process related information about new particle formation would require

1024   dedicated mechanistic experiments with more detailed information on particle precursors,

1025   ultrafine particles, and boundary layer mixing processes. DGR and MEV-types of new

1026   particle formation seem to be more closely related to near-surface processes. Thus, a low-

1027   level site such as the reopened Station Nord, (Nguyen et al., 2016), would be more suitable

1028   for related mechanistic experiments. Station Nord has the additional advantage of being close

1029   to the potential source regions of DGR and MEV-events identified by the present study.

1030   Acknowledgements

1031

1032   The back trajectories created through the local use of the HYSPLIT4 model developed,

1033   maintained and generously distributed by the Air Resources Laboratory of NOAA were a

1034   backbone of the present study. We are very grateful for the ceilometer data provided by the

1035   Alfred-Wegener- Institute in Bremerhaven/Potsdam and to NSIDC for their providing daily

1036   Arctic sea ice data. Complementing our own chemical analyses of Mt. Zeppelin filter data,

1037   sodium and sulfate results were taken from the EBAS database at the Norwegian Institute for

1038   Air Research (http://ebas.nilu.no), for which we are indebted to Anne-Gunn Hjellbrekke and

1039   Wenche Aas. We thank the NASA Ocean Biology Distributed Active Archive Center

1040   (OB.DAAC) for access to MODIS datasets. We are indebted to Yafang Cheng and Zhibin

1041   Wang for providing the algorithm for calculating the condensation sink. MG acknowledges

1042   the receipt of a Beatriu de Pinós post-doctoral fellowship funded by the Generalitat de

1043   Catalunya. Long-term funding oft he DMPS measurements was provided by the Swedish

1044   Environmental Protection Agency (Naturvårdsverket). We also thank Norwegian Polar

1045   Institute for substantial support oft the field operation on Mt. Zeppelin.

1046

1047

1048   Literature

1049

1050 Agarwal, J. K., and Sem, G. J.: Continuous flow, single-particle-counting condensation

1051   nucleus counter, J. Aerosol Sci., 11, 343-357, 1980.

1052 An, N., and Wang, K.: A Comparison of MODIS-Derived Cloud Fraction with Surface

1053   Observations at Five SURFRAD Sites, J. Appl. Meteor. Clim., 54, 1009-1020, 2015.

1054 Asmi, E., Kondratyev, V., Brus, D., Laurila, T., Lihavainen, H., Backman, J., Vakkari, V.,

1055   Aurela, M., Hatakka, J., Viisanen, Y., Uttal, T., Ivakhov, V., and Makshtas, A.:

1056   Aerosol size distribution seasonal characteristics measured in Tiksi, Russian Arctic,

1057   Atmos. Chem. Phys., 16, 1271-1287, 10.5194/acp-16-1271-2016, 2016.

1058 Ayers, G. P., Cainey, J. M., Granek, H., and Leck, C.: Dimethylsulfide oxidation and the ratio

1059   of methansulfonate to non sea-salt sulfate in the marine aerosol, J. Atmos. Chem., 25,

1060   307-325, 1996.

1061 Bates, T. S., Johnson, J. E., Quinn, P. K., Goldan, P. D., Kuster, W. C., Covert, D. C., and

1062   Hahn, C. J.: The biogeochemical sulfur cycle in the marine boundary layer over the

1063   Northeast Pacific Ocean, J. Atmos. Chem., 10, 59-81, 1990.

1064 Becagli, S., Lazzara, L., Marchese, C., Dayan, U., Ascanius, S. E., Cacciani, M., Caiazzo, L.,

1065   Di Biagio, C., Di Iorio, T., di Sarra, A., Eriksen, P., Fani, F., Giardi, F., Meloni, D.,

1066   Muscari, G., Pace, G., Severi, M., Traversi, R., and Udisti, R.: Relationships linking

1067   primary production, sea ice melting, and biogenic aerosol in the Arctic, Atmos.

1068   Environ., 136, 1-15, http://dx.doi.org/10.1016/j.atmosenv.2016.04.002, 2016.

1069 Beine, H. J., Argentini, S., Maurizi, A., Mastrantonio, G., and Viola, A.: The local wind field

1070   at Ny-Ålesund and the Zeppelin mountain at Svalbard, Meteorol. Atmos. Phys., 78,

1071   107–113, 2001.

1072 Bélanger, S., Babin, M., and Tremblay, J.-É.: Increasing cloudiness in Arctic damps the

1073   increase in phytoplankton primary production due to sea ice receding, Biogeosciences,

1074   doi:10.5194/bg-5110-4087-2013, 2013.

1075 Blanchard, D. C., and Woodcock, A. H.: Bubble formation and modification in the sea and its

1076   meteorological significance, Tellus, 9, 145-158, 1957.

1077 Browse, J., Carslaw, K. S., Mann, G. W., Birch, C. E., Arnold, S. R., and Leck, C.: The

1078   complex response of Arctic aerosol to sea-ice retreat, Atmos. Chem. Phys., 14, 7543-

1079   7557, 10.5194/acp-14-7543-2014, 2014.

1080 Charlson, R. J., Lovelock, J. E., Andreae, M. O., and Warren, S. G.: Oceanic phytoplankton,

1081   atmospheric sulphur, cloud albedo and climate, Nature, 326, 655-661, 1987.

1082 Croft, B., Martin, R. V., Leaitch, W. R., Tunved, P., Breider, T. J., D'Andrea, S. D., and
1083   Pierce, J. R.: Processes controlling the annual cycle of Arctic aerosol number and size
1084   distributions, Atmos. Chem. Phys., 16, 3665-3682, 10.5194/acp-16-3665-2016, 2016a.

1085 Croft, B., Wentworth, G. R., Martin, R. V., Leaitch, W. R., Murphy, J. G., Murphy, B. N.,
1086   Kodros, J. K., Abbatt, J. P. D., and Pierce, J. R.: Contribution of Arctic seabird-colony
1087   ammonia to atmospheric particles and cloud-albedo radiative effect, Nature
1088   Communications, 7, 13444, 10.1038/ncomms13444

1089 http://www.nature.com/articles/ncomms13444 - supplementary-information, 2016b.

1090 Dal Maso, M., Kulmala, M., Riipinen, I., Wagner, R., Hussein, T., Aalto, P. P., and Lehtinen,
1091   K. E. J.: Formation and growth of fresh atmospheric aerosols: eight years of aerosol
1092   size distribution data from SMEAR II, Hyytiälä, Finland, Bor. Env. Res., 10, 323-336,
1093   2005.

1094 Das, R., Granat, L., Leck, C., Praveen, P. S., and Rodhe, H.: Chemical composition of
1095   rainwater at Maldives Climate Observatory at Hanimaadhoo (MCOH), Atmos. Chem.
1096   Phys., 11, 3743-3755, 10.5194/acp-11-3743-2011, 2011.

1097 Dee, D. P., Uppala, S. M., Simmons, A. J., Berrisford, P., Poli, P., Kobayashi, S., and
1098   Bechtold, P.: The ERA‐Interim reanalysis: Configuration and performance of the
1099   data assimilation system, Q. J. Roy. Meteorol. Soc., 137, 553-597, 2011.

1100 Draxler, R., and Rolph, G.: HYSPLIT (HYbrid Single-Particle Lagrangian Integrated
1101   Trajectory) Model access via NOAA ARL READY, NOAA Air Resources
1102   Laboratory, Silver Spring, MD, 2003.

1103 Ehn, M., Vuollekoski, H., Petäjä, T., Kerminen, V.-M., Vana, M., Aalto, P., de Leeuw, G.,
1104   Ceburnis, D., Dupuy, R., O'Dowd, C. D., and Kulmala, M.: Growth rates during
1105   coastal and marine new particle formation in western Ireland, J. Geophys. Res., 115,
1106   n/a-n/a, 10.1029/2010JD014292, 2010.

1107 Flyger, H., and Heidam, N. Z.: Ground level measurements of the summer tropospheric
1108   aerosol in Northern Greenland, J. Aerosol Sci., 9, 157-168, 1978.

1109 Galí, M., Devred, E., Levasseur, M., Royer, S.-J., and Babin, M.: A remote sensing algorithm
1110   for planktonic dimethylsulfoniopropionate (DMSP) and an analysis of global patterns,
1111   Remote Sens. Environ., 171, 171-184, http://dx.doi.org/10.1016/j.rse.2015.10.012,
1112   2015.

1113 Galí, M., and Simó, R.: A meta‐analysis of oceanic DMS and DMSP cycling processes:
1114   Disentangling the summer paradox, Global Biochem. Cycles, 29, 496-515, 2015.

Gao, Q., Leck, C., Rauschenberg, C., and Matrai, P. A.: On the chemical dynamics of extracellular polysaccharides in the high Arctic surface microlayer, Ocean Sci. Discuss., 9, 215–259, 2012.

Heintzenberg, J., Bischof, W., Odh, S.-Å., and Moberg, B.: An investigation of possible sites for a background monitoring station in the European Arctic., International Meteorological Institute in Stockholm, Department of Meteorology, Stockholm University, Stockholm, Report Nr. AP-22, 74 pp, 1983.

Heintzenberg, J., and Larssen, S.: SO_2 and SO_4 in the Arctic: Interpretation of observations at three Norwegian Arctic-subArctic stations, Tellus, 35B, 255-265, 1983.

Heintzenberg, J.: Arctic haze: air pollution in polar regions, AMBIO, 18, 50-55, 1989.

Heintzenberg, J., and Leck, C.: Seasonal variation of the atmospheric aerosol near the top of the marine boundary layer over Spitsbergen related to the Arctic sulphur cycle, Tellus, 46B, 52-67, 1994.

Heintzenberg, J., Leck, C., Birmili, W., Wehner, B., Tjernström, M., and Wiedensohler, A.: Aerosol number-size distributions during clear and fog periods in the summer high Arctic: 1991, 1996, and 2001, Tellus, 58B, 41-50, 2006.

Heintzenberg, J., Wehner, B., and Birmili, W.: "How to find bananas in the atmospheric aerosol" New approach for analyzing atmospheric nucleation and growth events, Tellus B, 59, 273-282, 2007.

Heintzenberg, J.: The aerosol-cloud-climate conundrum, IJGW, 4, 219-241, 2012.

Heintzenberg, J., Leck, C., and Tunved, P.: Potential source regions and processes of aerosol in the summer Arctic, Atmos. Chem. Phys., 15, 6487-6502, 10.5194/acp-15-6487-2015, 2015.

Held, A., Brooks, I. M., Leck, C., and Tjernström, M.: On the potential contribution of open lead particle emissions to the central Arctic aerosol concentration, Atmos. Chem. Phys., 11, 3093-3105, 10.5194/acp-11-3093-2011, 2011a.

Held, A., Orsini, D. A., Vaattovaara, P., Tjernström, M., and Leck, C.: Near-surface profiles of aerosol number concentration and temperature over the Arctic Ocean, Atmos. Meas. Tech., 4, 1603–1616, 2011b.

Hubanks, P., Platnick, S., King, M., and Ridgway, B.: MODIS Atmosphere L3 Gridded Product Algorithm Theoretical Basis, Document (ATBD) and Users Guide, 2015.

Huschke, R. E.: Arctic cloud statistics from "air calibrated" surface weather observations, Rand Corporation Memo. RM 6173-PR, 79 pp, 1969.

1148   IOCCG: Ocean Colour Remote Sensing in Polar Seas, Report 16, Eds. Babin, M., Arrigo, K.,
1149   Bélanger, S. and Forget, M.-H., 129 pp, 2015.

1150   Jaenicke, R., and Schütz, L.: Arctic aerosols in surface air, Idöjaras, 86, 235-241, 1982.

1151   Junge, C. E.: Air chemistry and Radioactivity, Academic Press, New York and London, 382
1152   pp., 1963.

1153   Junninen, H., Hulkkonen, M., Riipinen, I., Nieminen, T., Hirsikko, A., Suni, T., Boy, M., Lee,
1154   S.-H., Vana, M., Tammet, H., Kerminen, V.-M., and Kulmala, M.: Observations on
1155   nocturnal growth of atmospheric clusters, Tellus B, 60, 365-371, 2008.

1156   Karl, M., Gross, A., Leck, C., and Pirjola, L.: Intercomparison of dimethylsulfide oxidation
1157   mechanisms for the marine boundary layer: Gaseous and particulate sulfur
1158   constituents, J. Geophys. Res., 112, D15304, 10.1029/2006JD007914, 2007.

1159   Karl, M., Leck, C., Gross, A., and Pirjola, L.: A Study of New Particle Formation in the
1160   Marine Boundary Layer Over the Central Arctic Ocean using a Flexible
1161   Multicomponent Aerosol Dynamic Model, Tellus, 64B,
1162   doi:http://dx.doi.org/10.3402/tellusb.v3464i3400.17158, 2012.

1163   Karl, M., Leck, C., Coz, E., and Heintzenberg, J.: Marine nanogels as a source of atmospheric
1164   nanoparticles in the high Arctic, Geophys. Res. Lett., 40, 3738–3743, DOI:
1165   10.1002/grl.50661, 2013.

1166   Keene, W. C., Pszenny, A. A. P., Galloway, J. N., and Hawley, M. E.: Sea-salt corrections
1167   and interpretation of constituent ratios in marine precipitation, J. Geophys. Res., 91,
1168   6647-6658, 1986.

1169   Keller, M. D., Bellows, W. K., and Guillard, R. R. L.: A survey of dimethylsulfide production
1170   in 12 classes of marine phytoplankton, in: Biogenic sulfur in the environment, edited
1171   by: E.S. Saltzman, and Cooper, W. J., American Chemical Society, Washington, D,
1172   167–182, 1989.

1173   King, M. D., Platnick, S., Menzel, W. P., Ackerman, S. A., and Hubanks, P. A.: Spatial and
1174   temporal distribution of clouds observed by MODIS onboard the Terra and Aqua
1175   satellites, IEEE Trans. Geosci. Remote Sens., 51, 3826–3852, 2013.

1176   Knutson, E. O., and Whitby, K. T.: Aerosol classification by electric mobility: apparatus,
1177   theory, and applications, J. Aerosol Sci., 6, 443-451, 1975a.

1178   Knutson, E. O., and Whitby, K. T.: Accurate Measurement of Aerosol Electrical Mobility
1179   Moments, J. Aerosol Sci., 6, 453-460, 1975b.

1180 Kulmala, M., Dal Maso, M., Mäkelä, J. M., Pirjola, L., Väkevä, M., Aalto, P. P.,
1181   Miikkulainen, P., Hämeri, K., and O'Dowd, C. D.: On the formation, growth and
1182   composition of nucleation mode particles, Tellus, 53B, 479-490, 2001.

1183 Kulmala, M., Vehkamäkia, H., Petäjä, T., Dal Maso, M., Lauri, A., Kerminen, V.-M., Birmili,
1184   W., and McMurry, P. H.: Formation and growth rates of ultrafine atmospheric
1185   particles: a review of observations, J. Aerosol Sci., 35, 143-176, 2004.

1186 Kulmala, M., Petäjä, T., Nieminen, T., Sipilä, M., Manninen, H. E., Lehtipalo, K., Dal Maso,
1187   M., Aalto, P. P., Junninen, H., Paasonen, P., Riipinen, I., Lehtinen, K. E. J.,
1188   Laaksonen, A., and Kerminen, V.-M.: Measurement of the nucleation of atmospheric
1189   aerosol particles, Nat. Protocols, 7, 1651-1667,
1190   http://www.nature.com/nprot/journal/v7/n9/abs/nprot.2012.091.html - supplementary-
1191   information, 2012.

1192 Lana, A., Simó, R., Vallina, S. M., and Dachs, J.: Re-examination of global emerging patterns
1193   of ocean DMS concentration, Biogeochem., 110, 173-182, 2012.

1194 Lannefors, H., Heintzenberg, J., and Hansson, H.-C.: A comprehensive study of physical and
1195   chemical parameters of the Arctic summer aerosol; results from the Swedish
1196   expedition Ymer-80, Tellus, 35B, 40-54, 1983.

1197 Leck, C., and Persson, C.: The central Arctic Ocean as a source of dimethyl sulfide: Seasonal
1198   variability in relation to biological activity, Tellus, 48B, 156-177, 1996a.

1199 Leck, C., and Persson, C.: Seasonal and short-term variability in dimethyl sulfide, sulfur
1200   dioxide and biogenic sulfur and sea salt aerosol particles in the arctic marine boundary
1201   layer, during summer and autumn, Tellus, 48B, 272-299, 1996b.

1202 Leck, C., and Bigg, E. K.: Aerosol production over remote marine areas - A new route,
1203   Geophys. Res. Lett., 23, 3577-3581, 1999.

1204 Leck, C., and Bigg, E. K.: New particle formation of marine biological origin, Aerosol Sci.
1205   Technol., 44, 570-577, 2010.

1206 Leck, C., Gao, Q., Mashayekhy Rad, F., and Nilsson, U.: Size-resolved atmospheric
1207   particulate polysaccharides in the high summer Arctic, Atmos. Chem. Phys., 13,
1208   12573-12588, 10.5194/acp-13-12573-2013, 2013.

1209 Lindsay, R., Wensnahan, M., Schweiger, A., and Zhang, J.: Evaluation of seven different
1210   atmospheric reanalysis products in the Arctic, J. Clim., 27, 2588-2606, 2014.

1211 Liss, P. S., and Merlivat, L.: Air-sea gas exchange rates: Introduction and synthesis, in: The
1212   Role of Air-Sea Exchange in Geochemical Cycling, edited by: Buat-Menard, P.,
1213   Reidel, Norwell, MS, 113-127, 1986.

1214   Maritorena, S., Siegel, D. A., and Peterson, A. R.: Optimization of a semianalytical ocean
1215   color model for global-scale applications, Appl. Opt., 41.15, 2705-2714, 2002.

1216   Matrai, P. A., and Vernet, M.: Dynamics of the vernal bloom in the marginal ice zone of the
1217   Barents Sea: Dimethyl sulfide and dimethylsulfoniopropionate budgets, Journal of
1218   Geophysical Research: Oceans, 102, 22965-22979, 10.1029/96JC03870, 1997.

1219   Nguyen, Q. T., Glasius, M., Sørensen, L. L., Jensen, B., Skov, H., Birmili, W., Wiedensohler,
1220   A., Kristensson, A., Nøjgaard, J. K., and Massling, A.: Seasonal variation of
1221   atmospheric particle number concentrations, new particle formation and atmospheric
1222   oxidation capacity at the high Arctic site Villum Research Station, Station Nord,
1223   Atmos. Chem. Phys., 16, 11319–11336, 10.5194/acp-2016-205, 2016.

1224   Norman, A. L., Barrie, L. A., Toom-Sauntry, D., Sirois, A., Krouse, H. R., Li, S. M., and
1225   Sharma, S.: Sources of aerosol sulphate at Alert: Apportionment using stable isotopes,
1226   J. Geophys. Res., 104, 11619-11631, 1999.

1227   O'Dowd, C., Monahan, C., and Dall'Osto, M.: On the occurrence of open ocean particle
1228   production and growth events, Geophys. Res. Lett., 37, L19805,
1229   doi:19810.11029/12010GL044679, 2010.

1230   Ogren, J. A., and Heintzenberg, J.: Parametric aerosol sampling at low concentration levels,
1231   Department of Meteorology, Stockholm UniversityAA-1, 1990.

1232   Orellana, M. V., Matrai, P. A., Janer, M., and Rauschenberg, C. D.:
1233   Dimethylsulfoniopropionate storage in *Phaecystis* (Prymnesiophyceae) secretory
1234   vesicles J. Phycol., 47, 112-117, 10.1111/j.1529-8817.2010.00936.x, 2011a.

1235   Orellana, M. V., Matrai, P. A., Leck, C., Rauschenberg, C. D., Lee, A. M., and Coz, E.:
1236   Marine microgels as a source of cloud condensation nuclei in the high Arctic, PNAS,
1237   108, 13612–13617, 2011b.

1238   Pierce, J. R., Westervelt, D. M., Atwood, S. A., Barnes, E. A., and Leaitch, W. R.: New-
1239   particle formation, growth and climate-relevant particle production in Egbert, Canada:
1240   analysis from 1 year of size-distribution observations, Atmos. Chem. Phys., 14, 8647-
1241   8663, 10.5194/acp-14-8647-2014, 2014.

1242   Pirjola, L., Kulmala, M., Wilck, M., Bischoff, A., Stratmann, F., and Otto, E.: Formation of
1243   sulphuric acid aerosols and cloud condensation nuclei: An expression for significant
1244   nucleation and model comparison, J. Aerosol Sci., 30, 1079-1094, 1999.

1245   Polissar, A. V., Hopke, P. K., Paatero, P., Kaufman, Y. J., Hall, D. K., Bodhaine, B. A.,
1246   Dutton, E. G., and Harris, J. M.: The aerosol at Barrow, Alaska: long-term trends and
1247   source locations, Atmos. Environ., 33, 2441-2458, 1999.

1248 Rahn, K. A., and Shaw, G. E.: Particulate air pollution in the Arctic: Large-scale occurence
1249   and meteorological controls, in: Atmospheric Aerosols and Nuclei, edited by: Roddy,
1250   F., and O'Connor, T. C., Dept. of Physics, University College, Galway, Ireland 21-27
1251   Sept., 223-227, 1977.

1252 Reischl, G. P.: Measurement of ambient aerosols by the differential mobility analyzer
1253   method: Concepts and realization criteria for the size range between 2 and 500 nm,
1254   Aerosol Sci. Tech., 14, 5-24, 1991.

1255 Ristovski, Z. D., Suni, T., Kulmala, M., Boy, M., Meyer, N. K., Duplissy, J., Turnipseed, A.,
1256   Morawska, L., and Baltensperger, U.: The role of sulphates and organic vapours in
1257   growth of newly formed particles in a eucalypt forest, Atmos. Chem. Phys., 10, 2919-
1258   2926, 10.5194/acp-10-2919-2010, 2010.

1259 Rudels, B., Björk, G., Nilsson, J., Winsor, P., Lake, I., and Nohr, C.: The interaction between
1260   waters from the Arctic Ocean and the Nordic Seas north of Fram Strait and along the
1261   East Greenland Current: results from the Arctic Ocean-02 Oden expedition, Journal of
1262   Marine Systems, 55, 1-30, 2005.

1263 Schmidtko, S., Johnson, G. C., and Lyman, J. M.: MIMOC: A global monthly isopycnal
1264   upper-ocean climatology with mixed layers, Journal of Geophysical Research:
1265   Oceans, 118, 1658-1672, 10.1002/jgrc.20122, 2013.

1266 Schoemann, V., Becquevort, S., Stefels, J., Rousseau, V., and Lancelot, C.: Phaeocystis
1267   blooms in the global ocean and their controlling mechanisms: a review, Journal of Sea
1268   Research, 53, 43-66, http://dx.doi.org/10.1016/j.seares.2004.01.008, 2005.

1269 Sharma, S., Chan, E., Ishizawa, M., Toom-Sauntry, D., Gong, S. L., Li, S. M., Tarasick, D.
1270   W., Leaitch, W. R., Norman, A., Quinn, P. K., Bates, T. S., Levasseur, M., Barrie, L.
1271   A., and Maenhaut, W.: Influence of transport and ocean ice extent on biogenic aerosol
1272   sulfur in the Arctic atmosphere, J. Geophys. Res., 117, D12209,
1273   10.1029/2011JD017074, 2012.

1274 Simó, R.: Production of atmospheric sulfur by oceanic plankton: biogeochemical, ecological
1275   and evolutionary links, Trends in Ecology & Evolution, 16, 287-294, 2001.

1276 Stohl, A.: Computations, accuracy and applications of trajectories - A review and
1277   bibliography, Atmos. Environ., 32, 947-966, 1998.

1278 Ström, J., Engvall, A.-C., Delbart, F., Krejci, R., and Treffeisen, R.: On small particles in the
1279   Arctic summer boundary layer: observations at two different heights near Ny-Ålesund,
1280   Svalbard, Tellus B - Chemical and Physical Meteorology, 61, 473-482, 2009.

1281 Suni, T., Kulmala, M., Hirsikko, A., Bergman, T., Laakso, L., Aalto, P. P., Leuning, R.,
1282   Cleugh, H., Zegelin, S., Hughes, D., van Gorsel, E., Kitchen, M., Vana, M., Hõrrak,
1283   U., Mirme, S., Mirme, A., Sevanto, S., Twining, J., and Tadros, C.: Formation and
1284   characteristics of ions and charged aerosol particles in a native Australian Eucalypt
1285   forest, Atmos. Chem. Phys., 8, 129-139, 10.5194/acp-8-129-2008, 2008.

1286 Tunved, P., Ström, J., and Krejci, R.: Arctic aerosol life cycle: linking aerosol size
1287   distributions observed between 2000 and 2010 with air mass transport and
1288   precipitation at Zeppelin station, Ny-Ålesund, Svalbard, Atmos. Chem. Phys., 13,
1289   3643–3660, 10.5194/acpd-12-29967-2012, 2013.

1290 Venzac, H., Sellegri, K., Villani, P., Picard, D., and Laj, P.: Seasonal variation of aerosol size
1291   distributions in the free troposphere and residual layer at the Puy de Dôme station,
1292   France, Atmos. Chem. Phys., 9, 1465-1478, 10.5194/acp-9-1465-2009, 2009.

1293 Warren, S. G., and Hahn, C. J.: Cloud climatology, in: Encyclopedia of Atmospheric
1294   Sciences, edited by: Holton, J. R., Pyle, J., and Curry, J. A., Academic Press, London,
1295   UK, 476-483, 2002.

1296 Wiedensohler, A., Covert, D., Swietlicki, E., Aalto, P., Heintzenberg, J., and Leck, C.:
1297   Occurrence of an ultrafine particle mode less than 20 nm in diameter in the marine
1298   boundary layer of the Arctic summer and autumn, Tellus, 48B, 213-222, 1996.

1299 Willis, M. D., Burkart, J., Thomas, J. L., Köllner, F., Schneider, J., Bozem, H., Hoor, P. M.,
1300   Aliabadi, A. A., Schulz, H., Herber, A. B., Leaitch, W. R., and Abbatt, J. P. D.:
1301   Growth of nucleation mode particles in the summertime Arctic: a case study, Atmos.
1302   Chem. Phys. Discuss., 2016, 1-31, 10.5194/acp-2016-256, 2016.

1303 Yli-Juuti, T., Riipinen, I., Pasi, A., Nieminen, T., Maenhaut, W., Janssens, A., Claeys, M.,
1304   Salma, I., Ocskay, R., Hoffer, A., Imre, K., and Kulmala, M.: Characteristics of new
1305   particle formation events and cluster ions at K-puszta, Hungary, Boreal Environment
1306   Research\, 14\, 2009.

1307 Young, L. H., Lee, S. H., Kanawade, V. P., Hsiao, T. C., Lee, Y. L., Hwang, B. F., Liou, Y.
1308   J., Hsu, H. T., and Tsai, P. J.: New particle growth and shrinkage observed in
1309   subtropical environments, Atmos. Chem. Phys., 13, 547-564, 10.5194/acp-13-547-
1310   2013, 2013.

1311 Zhang, M., Chen, L., Xu, G., Lin, Q., and Liang, M.: Linking Phytoplankton Activity in
1312   Polynyas and Sulfur Aerosols over Zhongshan Station, East Antarctica, J. Atmos. Sci.,
1313   72, 4629-4642, 2015.

1314

1315

1316

1317

Parameter	TR (h)	Explanation
C25	1 min	25% percentile of cloud base from AWI ceilometer (m)
CF12, 24, 36, 48, 5D	24	Average MODIS cloud fraction during the last 12h, 24h, 36, 48h, and days 3-5 before trajectory arrival
D50	1	Number-median diameter of particles < 50 nm diameter
CS	1	Condensation sink (s^{-1})
DZ	1	Vertical trajectory displacement $(m\ h^{-1})$ during the last hour before arrival
MSA	≥1 day	Methane sulfonate $(nmolm^{-3})$
N10	1	Number concentration of particles up to 10 nm $(>2010, cm^{-3})$
N20	1	Number concentration between 10 and 20 nm (cm^{-3})
N25	1	Number concentration of particles up to 25 nm (cm^{-3})
N40	1	Number concentration between 20 and 40 nm (cm^{-3})
N60	1	Number concentration between 40 and 60 nm (cm^{-3})
N100	1	Number concentration between 60 and 100 nm (cm^{-3})
N300	1	Number concentration between 100 and 300 nm (cm^{-3})
Na	≥1 day	Sodium concentrations $(nmolm^{-3})$
NCO	1	Number concentration of particles > 300 nm (cm^{-3})
$nssSO_4^{2-}$	≥1 day	Non-sea salt sulfate concentrations $(nmolm^{-3})$
NTO	1	Number concentration of particles ≥ 10 nm, $cm^{-3})$
OC12, 24, 36, 48, 5D	120	Average MODIS DMSPt (nmol) during the last 12h, 24h, 36, 48h, and days 3-5 before trajectory arrival
OW12, 24, 36, 48, 5D	24	Average open water (%) during the last 12h, 24h, 36, 48h, and days 3-5 before trajectory arrival
PRE	1	Trajectory precipitation (mm) at arrival
RH	1	Trajectory relative humidity (%) at arrival
SFL	1	Solar flux at trajectory arrival (Wm^{-2})
SP12, 24, 36, 48, 5D	1	Accumulated precipitation (mm) during the last 12h, 24h, 36, 48h, and days 3-5 before trajectory arrival
T12, 24, 36, 48, 5D	24	Average sea surface temperature (C) during the last 12h, 24h, 36, 48h, and days 3-5 before trajectory arrival
TEM	1	Trajectory temperature (C) at arrival
WDR	1	Trajectory wind direction (°) during the last hour before arrival
WSP	1	Trajectory wind speed $(m\ sec^{-1})$ during the last hour before arrival

1318
1319   Table 1 Aerosol, atmospheric, and ocean parameters utilized in the present study.

1320   DMSPt = Total dimethylsulfoniopropionate in surface ocean waters. TR = temporal

1321   resolution in which the respective data were available. All parameter explanations

1322   starting with "Trajectory" refer to parameters calculated by HYSPLIT4 at each

1323   trajectory step.

1324

1325

1326

1327

1328

1329

1330

1331

1332

Approach	Acronym	Criteria and thresholds	Total number of events	Number of unique events	% of total number of data hours
Percentiles	PCT	N25 >93%-percentile	4143	240	1
Diameter-growth	DGR	D50-Growth >1.5	1199	235	3
Multi-size growth	MEV	Multi-growth >1.6	1191	266	4
Sum			6533	741	

1333

1334   Table 2 Total and unique number of events of new particle formation identified by the three

1335   approaches to identify NPF-events, and percent of all data hours covered by unique

1336   events.

1337

1338

Statistics	J11	GR11	J22	GR22
Minimum	0.1	-1.2	0.1	-0.1
25%	0.4	0.1	0.2	1.0
50%	0.7	0.4	0.3	1.4
75%	1.4	0.6	0.7	1.8
Maximum	19	2.2	22	4

1339

1340   Table 3 Statistics of particle formation rates of DGR-events J11, and J22, ($cm^{-3}s^{-1}$), at the

1341   nominal geometric mean diameters 11 nm, and 22 nm and corresponding diameter

1342   growth rates GR11, and GR22, (nmh^{-1}) in the two diameter ranges 5 – 25 nm, and

1343   10 – 50 nm.

1344
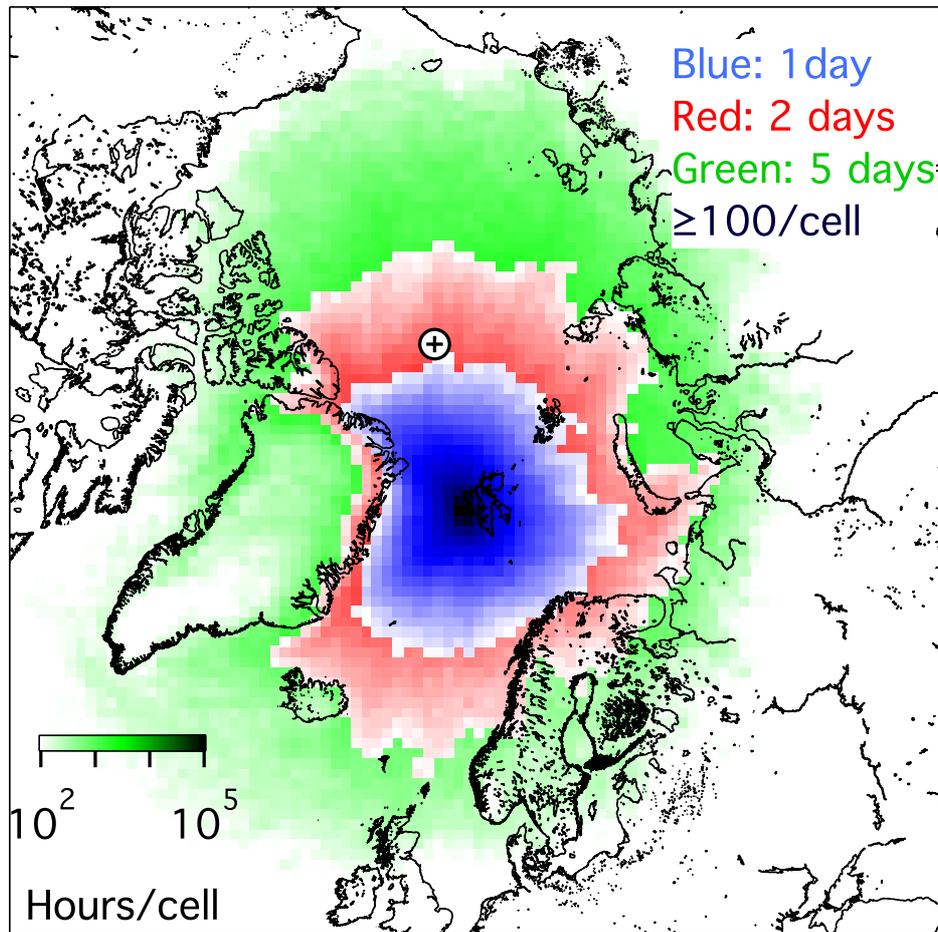
1345

1346   Fig. 1   Map of the regional distribution of 5-day (green), 2-day (red), and 1-day (blue)

1347   hourly back trajectories to Mt. Zeppelin during the months March through October

1348   of the years 2006 - 2015. Black symbol: North Pole. The colored areas are covered

1349   with at least 100 trajectory hours per geocell and the color saturation corresponds to

1350   the number of trajectory hours per grid cell on a log-scale.

1351
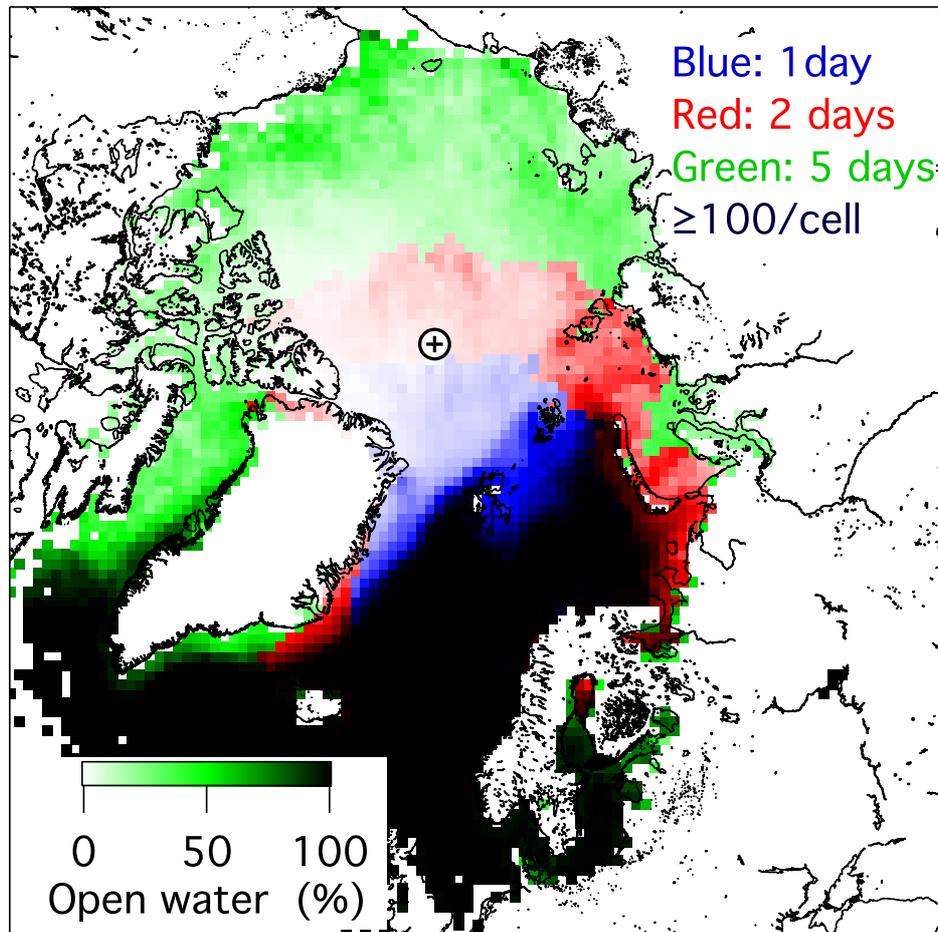
1352

1353   Fig. 2   Map of the regional distribution of open water under 87648 5-day (green), 2-day

1354   (red), and 1-day (blue) hourly back trajectories to Mt. Zeppelin during the during the

1355   months March through October of the years 2006-2015. Black symbol: North Pole.

1356   The areas are covered with at least 100 trajectory hours concurrent with data values

1357   per geocell.

1358

1359

Fig. 3   Map of the regional distribution of DMSPt along 87648 5-day (green), 2-day (red),

and 1-day (blue) hourly back trajectories to Mt. Zeppelin during the during the

months March through October of the years 2006-2015. Black symbol: North Pole.

The relative color scale holds for all colors. The areas are covered with at least 100

trajectory hours with data values per geocell.

1365
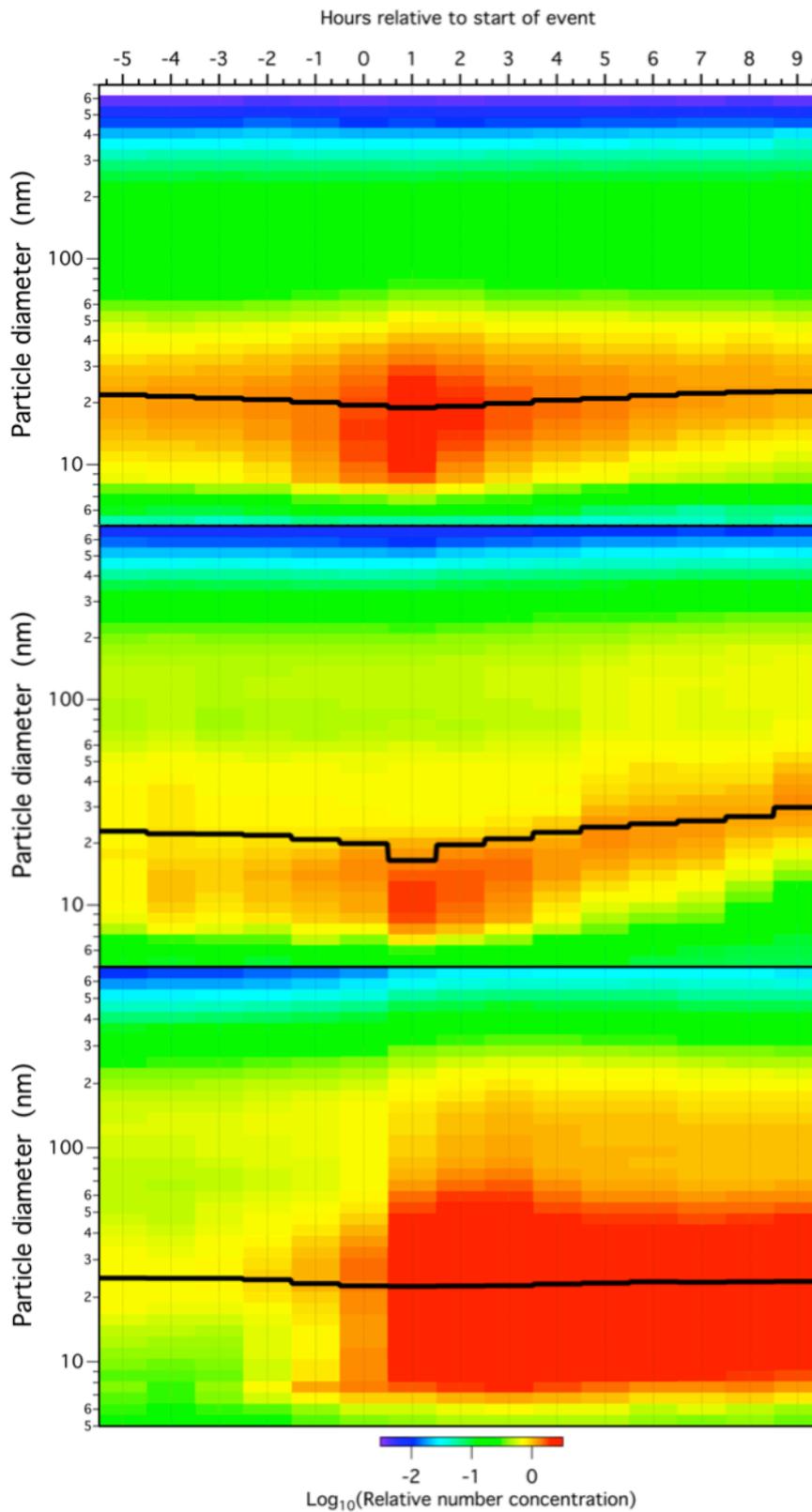
1366

1367   Fig.4   Average temporal development of the relative number size distribution before and

1368   during NPF-events identified by the three approaches. Relative number

1369   concentrations are formed by dividing absolute number concentrations by the

1370   average total number during the six-hour pre-event time periods. The black curve

1371   gives the median sub-50-nm particle diameter D50 during the events. Top: PCT-

1372   events; center: DGR-events; bottom: MEV-events.

1373
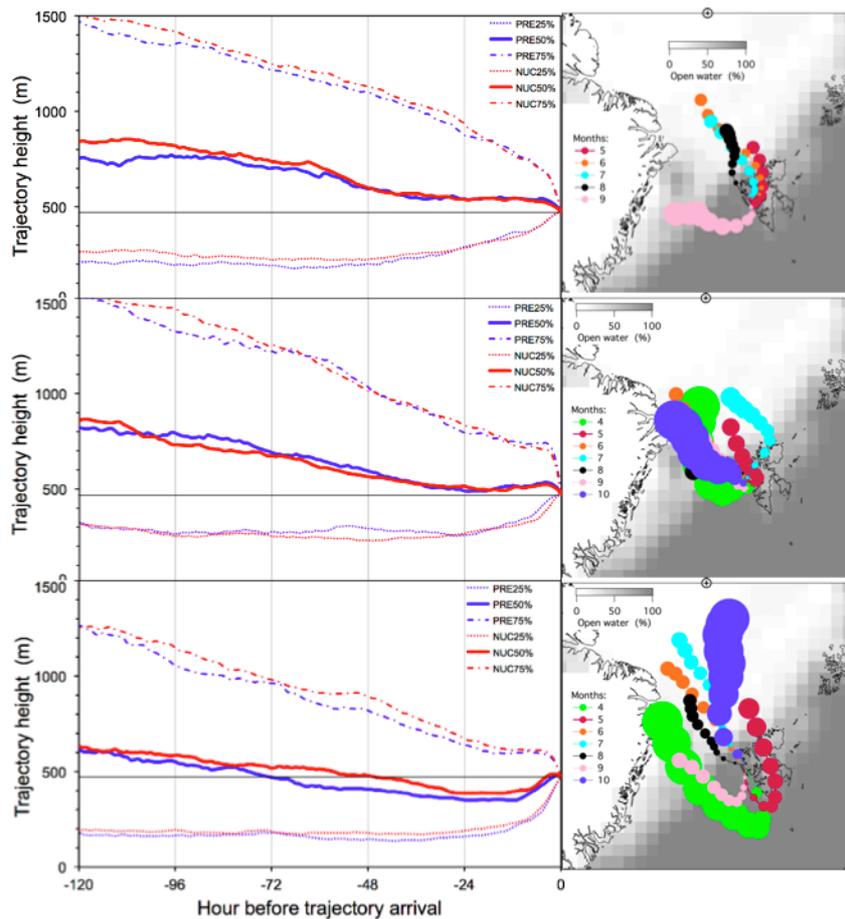
1374

Fig. 5   Left panels: Median back trajectory height profiles (m) during the six pre-event hours (full line in blue, PRENUC) and during the nine DGR-event hours (full line in red, NUC). 25% and 75% percentiles are shown as dotted, and dash-dotted lines, respectively. Top: PCT-events; center: DGR-events; bottom: MEV-events. The thin horizontal line marks the station level.

Right panels: Average monthly trajectory positions in 12 h steps for the months April though October. Only months with at least 10 NPF-events are shown. The circles comprise 95% of all trajectories at any trajectory step. The underlying grey-scale map indicates July ice cover averaged over the years 2006 – 2015
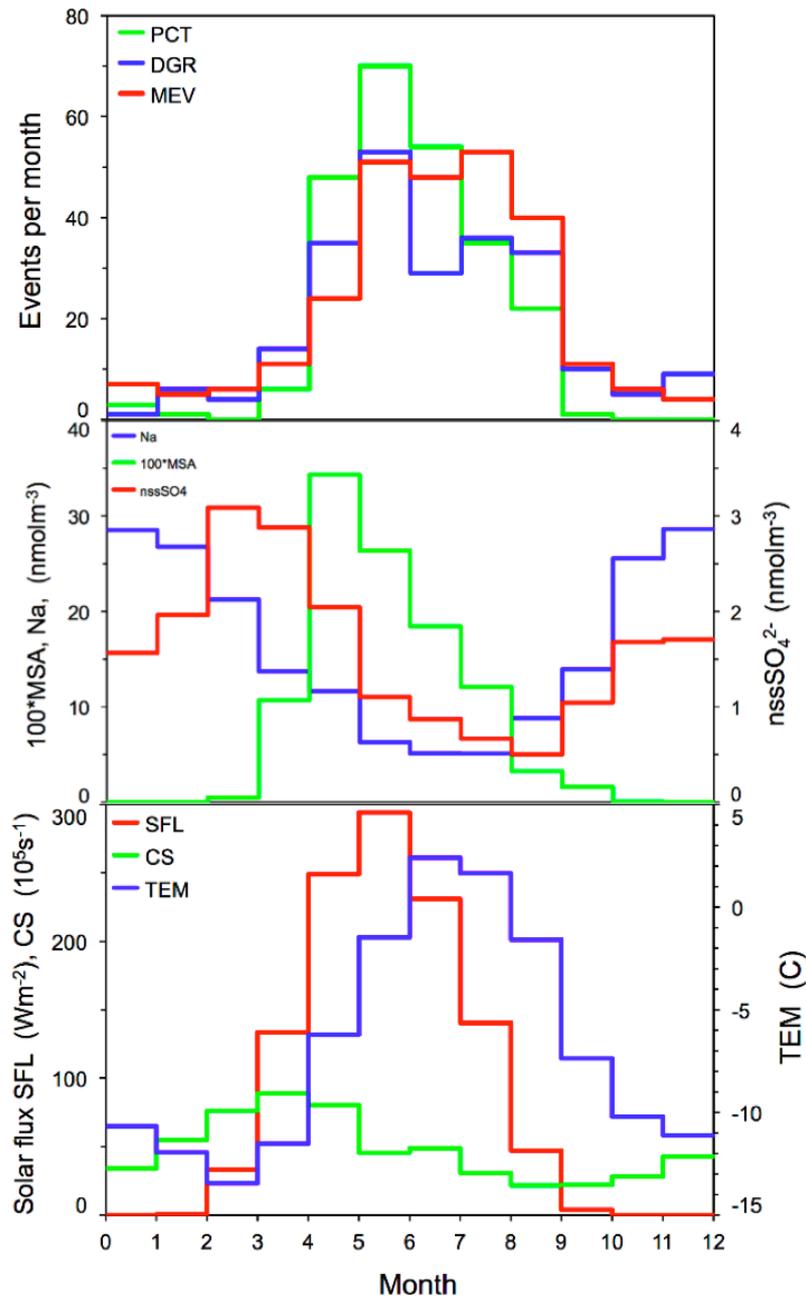
1385

1386   Fig. 6   Top: Monthly numbers of new particle formation events according to the three

1387   approaches, summed up over the whole period of ten years. PCT: Upper percentile

1388   of N25; DGR: Diameter growth; MEV: Multiple size events.

1389   Center: Average seasonal distribution of particle composition in $nmolm^{-3}$.

1390   Na = sodium, nssSO4 = $nssSO_4^{2-}$, MSA = Methane sulfonate times 100.

1391   Bottom: Monthly average solar flux (SFL, red, Wm^{-2}), and temperature (TEM, blue

1392   °C), and condensation sink, (CS, $10^5 s^{-1}$), at Mt. Zeppelin, Spitsbergen.

1393

1394
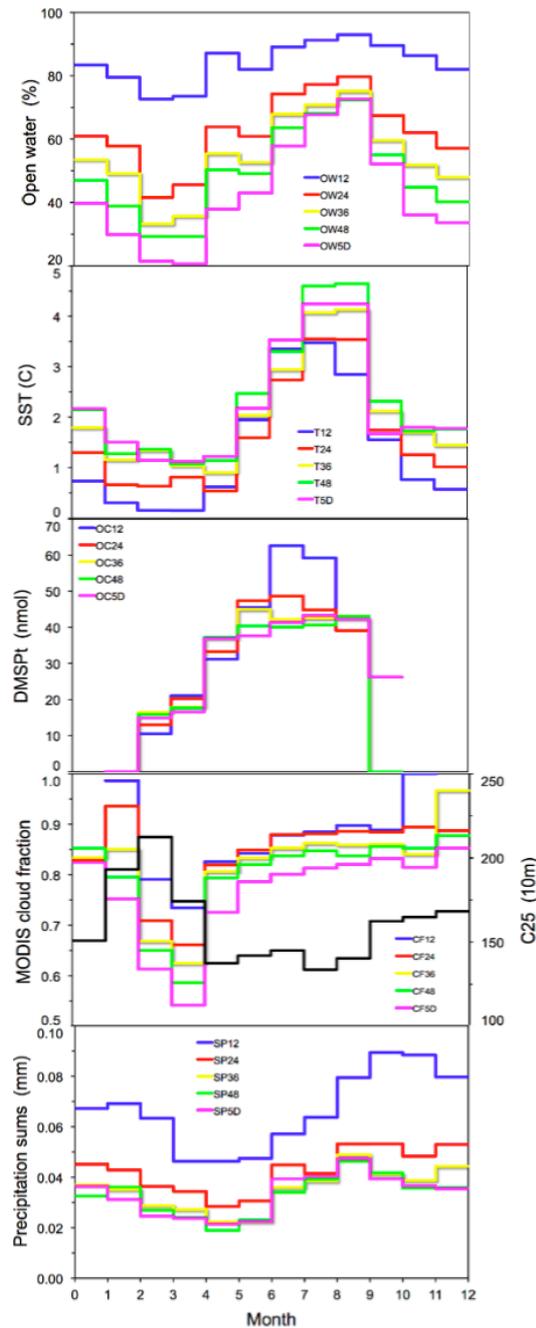
1395

1396   Fig. 7   Monthly averages of environmental parameters averaged along back trajectories to

1397   Mt. Zeppelin. From top to bottom: OW12-5D: Open water in % during last 12, 24,

1398   36, and 48h, and days 3-5 before trajectory arrival at Mt. Zeppelin. T12-5D: Same

1399   for sea surface temperature in °C. OC12-5D: Same for DMSPt in nmol in surface

1400   waters.   CF12-5D: Same for MODIS cloud fraction.   SP12-5D: Same for

1401   precipitation sums in mm. C25 = 25%-percentile of cloud base in decameter.

1402
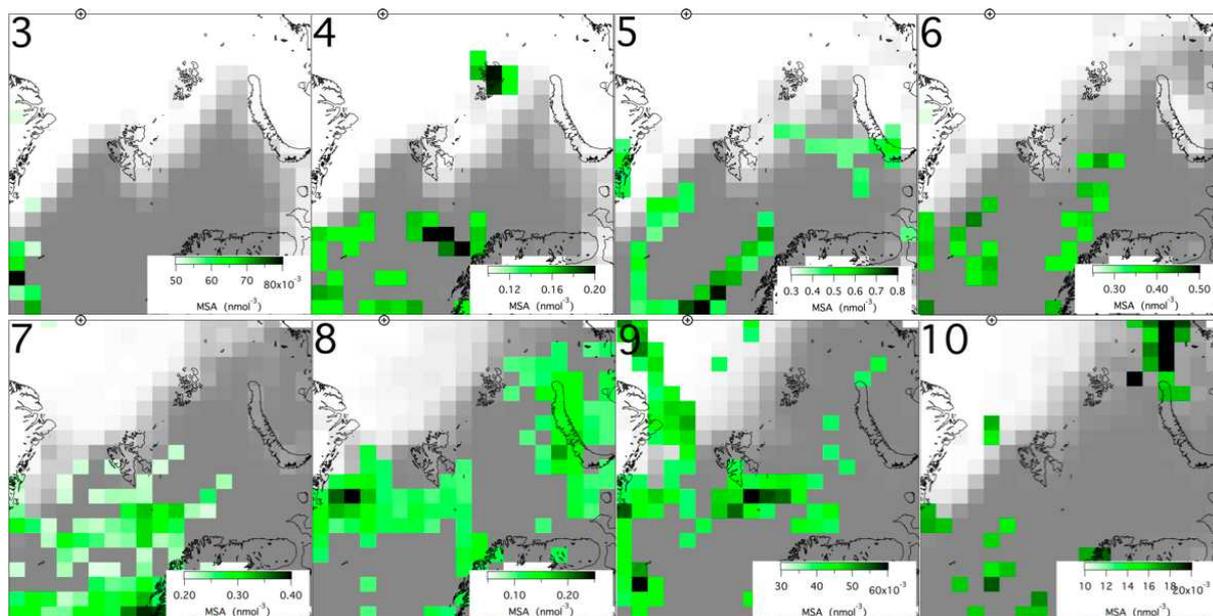
1403

1404   Fig. 8   Average monthly distribution of methane sulfonic acid, (MSA, nmolm^{-3}), during the

1405   months March – October of the years 2006 – 2015, constructed from MSA-

1406   concentrations measured on Mt. Zeppelin, which were extrapolated along 5-day back

1407   trajectories.   Average open water percentages during the respective months are

1408   indicated as white (0% open water) to dark grey (100% open water) areas.   The

1409   position of the North Pole is marked as cross in circle on the upper border of the

1410   maps.

1411
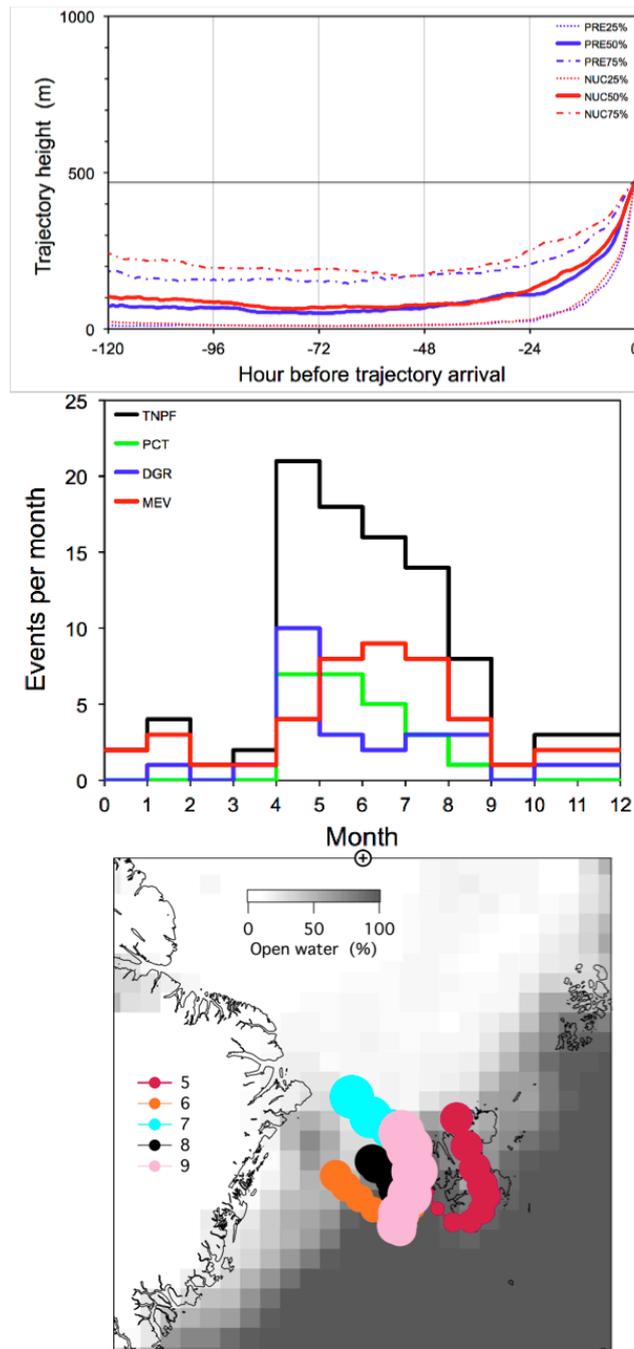
1412

1413   Fig. 9   Characteristics of the subpopulation of 93 NPF-events with back trajectories that

1414   stayed below 500 m for five days before arrival. Top: Statistics of related vertical

1415   trajectory coordinates as in Fig. 5. Center: Average monthly occurrence of PCT,

1416   DGR, and MEV-events, summed up over the whole period of ten years. Bottom:

1417   Related average monthly trajectory positions in 12 h steps for the months May

1418   through September. The circles comprise 95% of all trajectories at any trajectory

1419   step. The underlying grey-scale map indicates July ice cover averaged over 2006 –

1420   2015.

1421
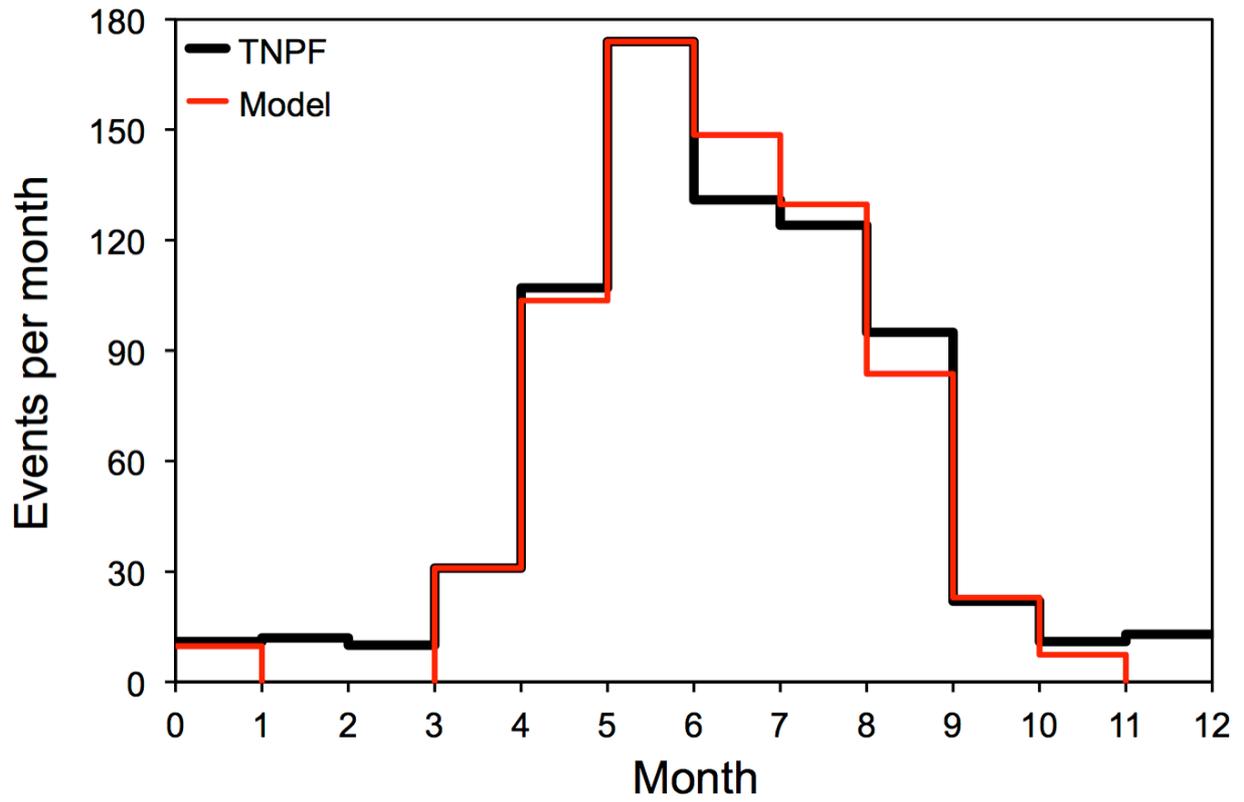
1422

1423   Fig. 10 Average monthly sums of NPF-events due to the three types of new particle

1424   formation, (TNPF, black), summed up over the whole period of ten years. Red:

1425   Three-parameter model to describe TNPF.

1426
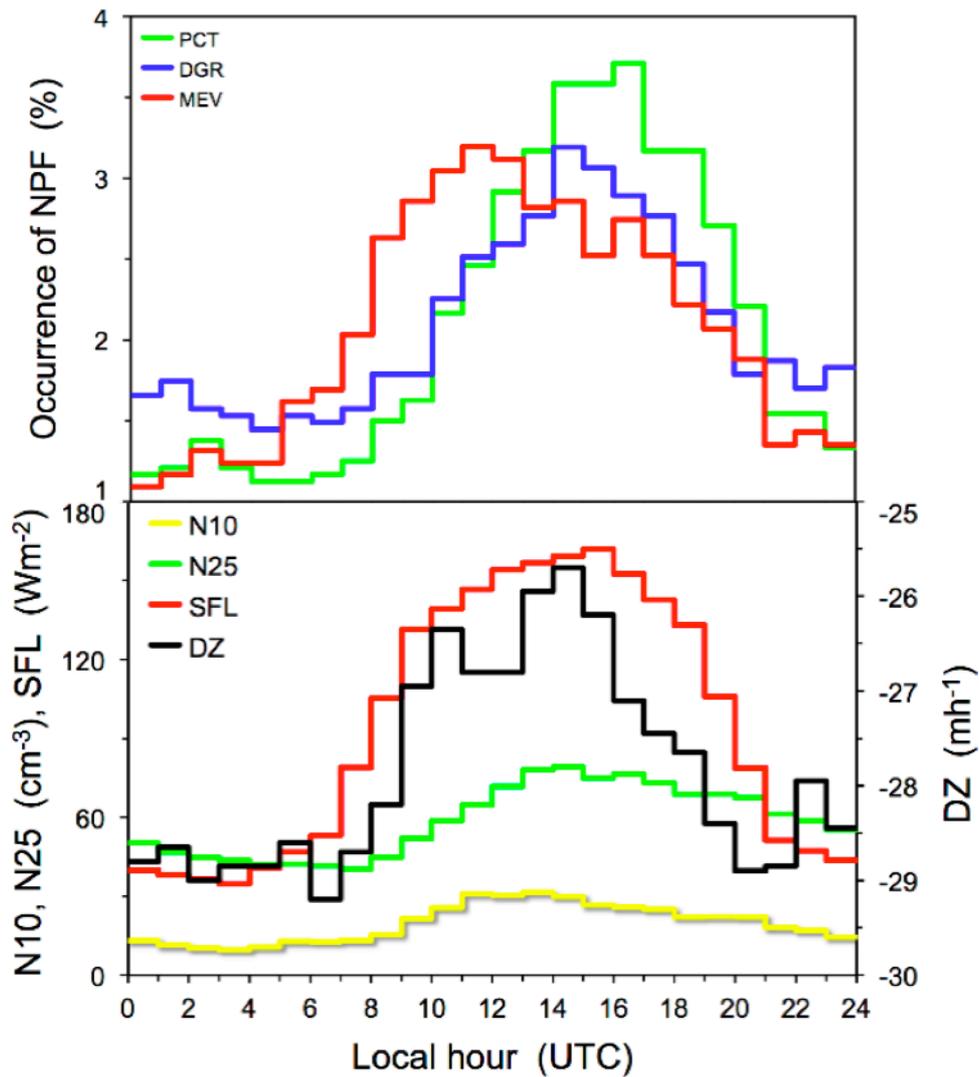
1427

1428   Fig. 11   Top: Relative average diurnal occurrence of the three types NPF-events.   PCT:

1429   Upper percentile of N25; DGR: Diameter growth; MEV: Multiple size events.

1430   Bottom: Average diurnal variation of the HYSPLIT-modeled solar flux (SFL, Wm^{-2}),

1431   the integral particle concentrations N10, and N25 in cm^{-3}, and of the vertical

1432   displacement parameter (DZ, mh^{-1}).   N10 is based on data of the years 2011 – 2015

1433   whereas the other parameters are based on data of the years 2006 – 2015.